J. Fluid Mech. (1985), *vol.* 153, *pp.* 31–58
Printed in Great Britain

Higher-order derivative correlations and the alignment of small-scale structures in isotropic numerical turbulence

By ROBERT M. KERR
NASA Ames Research Center, M.S. 202A-1, Moffett Field, CA 94035

(Received 6 September 1983 and in revised form 25 May 1984)

In a three-dimensional simulation higher-order derivative correlations, including skewness and flatness (or kurtosis) factors, are calculated for velocity and passive scalar fields and are compared with structures in the flow. Up to 128^3 grid points are used with periodic boundary conditions in all three directions to achieve R_λ to 82.9. The equations are forced to maintain steady-state turbulence and collect statistics. The scalar-derivative flatness is found to increase much faster with Reynolds number than the velocity-derivative flatness, and the velocity- and mixed-derivative skewnesses do not increase with Reynolds number. Separate exponents are found for the various fourth-order velocity-derivative correlations, with the vorticity-flatness exponent the largest. This does not support a major assumption of the lognormal and β models, but is consistent with some aspects of structural models of the small scales. Three-dimensional graphics show strong alignment between the vorticity, rate-of-strain, and scalar-gradient fields. The vorticity is concentrated in tubes with the scalar gradient and the largest principal rate of strain aligned perpendicular to the tubes. Velocity spectra, in Kolmogorov variables, collapse to a single curve and a short $-\frac{5}{3}$ spectral regime is observed.

1. Introduction

The classical approach to investigating small-scale intermittency in turbulence is through the higher-order derivative correlations such as skewness and flatness factors. Experimentally this has been done for both velocity and temperature, which is a passive scalar when buoyancy is negligible. The long-range goal is to improve our understanding of the structure of the small scales, possibly leading to improved methods for subgrid modelling. An intermediate objective has been to relate the derivative correlations to dissipation correlations and corrections to Kolmogorov scaling. It is believed that this is possible because the small scales are universal; that is, the small scales have a structure that is independent of the large scales and can be modelled. Hot-wire measurements of higher-order velocity and scalar statistics with one velocity component, such as the velocity-derivative flatness and skewness, support this conclusion. More complicated statistics have not been measured and alternative approaches, such as flow visualization, are limited because they do not have the flexibility necessary to distinguish small-scale structures that are intermittent in space and time.

Another approach to investigating the small scales is numerical simulations, which can provide more detail than experiments. For example, because all components of the velocity are known in a simulation, one is able to study correlations beyond the

derivative skewness and flatness and computer graphics can display structures not accessible to experiments. The main disadvantage of a simulation is that only a limited range of lengthscales is allowed, which restricts the Reynolds number to very low values. But in low-Reynolds-number experiments the values of most of the derivative correlations are significantly different from their uncorrelated or Gaussian values. Therefore, these statistics are accessible to current numerical methods and computers. Siggia (1981*a*) used a numerical simulation to calculate higher-order correlations of the velocity, and discussed the relation between small-scale vortex structures and intermittency. Our approach will be to use a similar simulation to look in more detail at the velocity-derivative statistics and the statistics of a passive scalar. Graphical display of small-scale vorticity, rate-of-strain, and scalar-gradient structures is used to interpret these statistics and comparisons with phenomenological theories and experiments are made.

There are two phenomenological approaches to predicting the small-scale statistics: either by assuming a form for vortical structures or a form for the energy cascade from large to small scales. Two models that are based on the cascade of energy are the lognormal theory of Kolmogorov (1962) and the β-model of Frisch, Sulem & Nelkin (1979). Both theories predict a correction to the $k^{-\frac{5}{3}}$ inertial-range kinetic-energy spectrum of Kolmogorov (1941). They also predict that as the Reynolds number grows the velocity fluctuations become increasingly localized, or intermittent, distributions become highly non-Gaussian, and the higher-order correlations, such as the derivative skewness and flatness factors, increase with Reynolds number with a power-law dependence. The power-law exponents depend on the details of each model and on μ, the characteristic exponent of the dissipation–dissipation correlation function in the inertial subrange $\eta \ll r \ll L$:

$$\langle \epsilon(x)\,\epsilon(x+r)\rangle = A\epsilon^2 \left(\frac{L}{r}\right)^{\mu} \tag{1}$$

(Monin & Yaglom 1975, p. 618), where A is a constant and L is defined by (12). All correlations of a given order are predicted to have the same power-law dependence. The lognormal model predicts that

$$\langle \epsilon^m(x)\,\epsilon^n(x+r)\rangle \sim \left(\frac{L}{r}\right)^{\mu mn}, \tag{2}$$

and that

$$F_{\partial u^n} = \frac{\left\langle \left(\dfrac{\partial u_1}{\partial x_1}\right)^n \right\rangle}{\left\langle \left(\dfrac{\partial u_1}{\partial x_1}\right)^2 \right\rangle^{\frac{1}{2}n}} \sim R_\lambda^{\alpha_n}, \tag{3}$$

where

$$\alpha_n = \tfrac{3}{4}\mu n(n-1) \tag{4}$$

(Frenkiel & Klebanoff 1975). The β-model is similar, but predicts that

$$\alpha_n = \frac{3\mu}{4-\mu}\left(\frac{n}{2}-1\right) \tag{5}$$

(Nelkin & Bell 1978). The success of these models in predicting the experimentally observed dependence of derivative skewness and flatness on Reynolds number is discussed in detail by Antonia, Satyaprakash & Hussain (1982), who conclude that the lognormal model is superior in this respect. Neither of the corrections to the $k^{-\frac{5}{3}}$

law proposed has been observed, although the lognormal correction is much smaller and probably not much above statistical noise.

The value of μ can be found either from the spectra of squared velocity derivatives or by using these models to calculate back from α_n. Nelkin (1981) and Antonia *et al.* (1982) summarize the current experimental values for μ, but, because calculating μ depends on the model used and experiments conflict, we calculate only the α_n.

Structural models assume that the small scales are composed of tubes or sheets of vorticity. Corrsin (1962) assumed that sheets dominated and concluded that $\alpha_4 = 1.5$. Saffman (1968) also assumed that the vorticity would be found in sheets whose thickness would be the order of the Taylor microscale (9), but that, within the sheets, dissipation would be localized in regions characterized by the Kolmogorov lengthscale (10*a*). He found that $\alpha_4 = 1$ and $\alpha_3 = 0$, that is, the skewness is constant. A variation, proposed by Tennekes (1968), assumes that the dominant structures are tubes whose thickness is the Kolmogorov lengthscale, but which are subject only to the large-scale strain. His results agree with those of Saffman. Experimentally, α_3 is observed to be very small, possibly zero, but α_4 is much less than the predicted value of 1.

Dissipation of the variance of a passive scalar is observed to be intermittent, much like kinetic-energy dissipation. For example, the scalar-derivative flatness scales with Reynolds number in a manner similar to the velocity-derivative flatness, but with a larger exponent (Antonia & Chambers 1980). Sudden jumps in experimental temperature signals, known as 'ramps', are also observed (Antonia *et al.* 1979). The only theoretical attempt to describe scalar intermittency was by Van Atta (1974), who used lognormal assumptions. Correlations between the velocity and scalar derivatives would also be interesting, but because it is difficult to measure two turbulent fields simultaneously, there have been almost no experimental measurements of these correlations.

In this paper, a variety of velocity- and scalar-derivative correlations are calculated over a range of Reynolds numbers. In an isotropic uncorrelated field with Gaussian statistics each of the correlations to be discussed has an easily determined value. For the velocity-derivative correlations $F_{\partial u^n}$ (3), the skewness ($n = 3$) is zero, the flatness ($n = 4$) is 3, and the sixth-order correlation is 15. For mixed correlations in which both the velocity derivative and the scalar derivative have a power of 2, such as the mixed-derivative correlation (40), the uncorrelated value is 1. At high Reynolds numbers the statistics are usually highly non-Gaussian, both in experiments and in our simulations. We will concentrate on third- and fourth-order correlations, with some fifth- and sixth-order correlations presented to allow comparisons with the phenomenological models. Since the models discussed predict scaling laws and exponents, we will estimate these exponents and make comparisons.

The governing equations are the incompressible Navier–Stokes equation for the velocity and the transport equation for a passive scalar. The Navier–Stokes equation is

$$\frac{\partial \boldsymbol{u}}{\partial t} + \boldsymbol{u}\cdot\boldsymbol{\nabla}\boldsymbol{u} = -\frac{\boldsymbol{\nabla} p}{\rho} + \nu \boldsymbol{\nabla}^2 \boldsymbol{u}, \tag{6a}$$

$$\boldsymbol{\nabla}\cdot\boldsymbol{u} = 0 \quad \text{(incompressibility)}.$$

The nonlinear term, $\boldsymbol{u}\cdot\boldsymbol{\nabla}\boldsymbol{u}$, can be written in several different forms which are computationally convenient: the conservative form,

$$\boldsymbol{\nabla}\cdot(\boldsymbol{u}\boldsymbol{u}), \tag{6b}$$

and the rotational form,

$$\boldsymbol{\omega}\times\boldsymbol{u} + \boldsymbol{\nabla}\tfrac{1}{2}u^2. \tag{6c}$$

The scalar equation can also be written two ways in incompressible flow: the convective form

$$\frac{\partial\theta}{\partial t}+\boldsymbol{u}\cdot\boldsymbol{\nabla}\theta = D\nabla^2\theta, \tag{7a}$$

and the conservative form

$$\frac{\partial\theta}{\partial t}+\boldsymbol{\nabla}\cdot\boldsymbol{u}\theta = D\nabla^2\theta. \tag{7b}$$

In the absence of viscosity ν and diffusivity D the equations conserve two positive-definite quadratic invariants: the kinetic energy of turbulent fluctuations

$$E = \tfrac{1}{2}\langle u_i u_i\rangle,$$

and the scalar variance

$$E_\theta = \langle\theta^2\rangle.$$

The fundamental dimensionless parameters that determine our statistics are the Taylor-microscale Reynolds number $R_\lambda = U\lambda/\nu$ and the Prandtl number ν/D, where U is the characteristic velocity of the turbulence,

$$\tfrac{3}{2}U^2 = E, \tag{8}$$

and λ is the Taylor microscale,

$$\lambda = \frac{\langle u_1^2\rangle^{\frac{1}{2}}}{\langle(\partial u_1/\partial x_1)^2\rangle^{\frac{1}{2}}}. \tag{9}$$

Also of interest are the kinetic-energy dissipation rate,

$$\epsilon = -\frac{\mathrm{d}}{\mathrm{d}t}\langle\tfrac{3}{2}U^2\rangle,$$

and the scalar-variance dissipation rate,

$$\chi = -\frac{\mathrm{d}}{\mathrm{d}t}\langle\theta^2\rangle.$$

The Kolmogorov lengthscale, wavenumber cutoff, and velocity scale are defined as

$$\eta = \left(\frac{\nu^3}{\epsilon}\right)^{\frac{1}{4}}, \quad K_\mathrm{k} = \frac{1}{\eta}, \quad \text{and} \quad (\epsilon\nu)^{\frac{1}{4}}, \tag{10a}$$

and the Oboukov–Corrsin microscale and wavenumber (Corrsin 1951) are defined as

$$\eta_\mathrm{OC} = \left(\frac{D^3}{\epsilon}\right)^{\frac{1}{4}} \quad \text{and } K_\mathrm{OC} = \frac{1}{\eta_\mathrm{OC}}. \tag{10b}$$

2. Numerical method

Two numerical codes were used for the simulations presented. Each is a three-dimensional spectral code with periodic boundary conditions. By spectral we mean that the fundamental variables that are stored and advanced in time are the Fourier-transformed velocity and scalar fields $u(k)$ and $\theta(k)$. For simple geometries these methods allow more resolution than finite-difference methods for the same number of grid points (Orszag 1971). To improve the speed of spectral methods fast Fourier transforms are used to return to physical space, where the nonlinear terms are calculated by forming products. This method is sometimes referred to as pseudospectral because it introduces aliasing errors in the high wavenumbers. One way to reduce these errors, or dealias, is by truncating interactions outside a

boundary in Fourier space. This does not significantly affect the resolution because only the high-wavenumber tail of the spectrum, with only a small fraction of the total energy, is truncated. To completely dealias one should truncate all wavenumbers larger than $\frac{1}{3}N$, where N is the number of grid points in a single direction. To completely dealias a three-dimensional code without truncation requires calculating the nonlinear terms on eight shifted grids. Fortunately, Patterson & Orszag (1971) have shown that in two or more dimensions all the aliasing errors can be eliminated by using only two shifted grids and a spherical truncation with the proper radius. This method was used in their original code, known as Superbox. Another approach uses shifted grids on alternate evaluations (Rogallo 1981). The extent to which aliasing errors affect a calculation also depends on the algorithm used for the convective terms. Superbox uses the aliased rotation algorithm (6*c*) because it conserves kinetic energy, which helps inhibit instabilities and reduces the need for using shifted grids. To determine whether a dealiasing scheme is actually reducing errors can only be determined by numerical tests. For sufficiently strong dissipation aliasing errors are very small and it is difficult to determine if a scheme is better. For example, comparisons between versions of Superbox with and without shifted grids show no significant differences in their spectra when dissipation is strong (G. S. Patterson, National Center for Atmospheric Research, private communication 1980).

The scalar equations do not allow aliasing to be neglected as easily as the Navier–Stokes equations do. For zero diffusivity, the scalar variance is conserved by the exact equations. But the aliased versions of both the convective and conservative equations (7*a*, *b*) do not conserve scalar variance. Instead, their respective aliasing errors are equal in magnitude and opposite in sign. We investigated taking advantage of this by averaging the two forms of the scalar equation to dealias, but it did not yield any significant improvements because our fields were already well resolved.

The code used for the 32^3 runs is based on the Superbox code of Siggia & Patterson (1978) and Siggia (1981*a*). The rotational form of the Navier–Stokes equation (6*c*) was used for the velocity and the time advancement was leapfrog with stabilization done every 40 time-steps by a second-order Runge–Kutta step. Shifted grids were not used for dealiasing, but the convective and conservative forms of the scalar equation (7*a*, *b*) were used on alternate time-steps to partially dealias the scalar. Wavenumbers were truncated outside a sphere of radius $\frac{1}{2}N$. This truncation has the advantage of being isotropic, but does allow significant one-dimensional aliasing errors. Details of this code may be found in Kerr (1981). Simulation of the velocity and one scalar required approximately 0.75 s of computer time (c.p.u.) per evaluation on a Cray-1S computer and the longest simulation used 40 min of computer time.

The code for the 64^3 and 128^3 calculations also used the rotational form of the Navier–Stokes equations, with a spherical truncation of $\frac{1}{2}N$ and without shifted grids, but only the conservative form of the scalar equation was used. The time advancement was third-order Runge–Kutta (A. Wray, NASA Ames Research Center, private communication, 1981) and up to three scalars could be calculated simultaneously. For a 64^3 mesh with three scalars, 6.5 s of Cray c.p.u. were required for each evaluation, with three evaluations per time-step. The code with no scalars required 3.25 s of c.p.u. per evaluation. Our longest simulation for a 64^3 mesh with three scalars (F19-21) required 12 h of computer time to simulate seven eddy-turnover times (11). For a 128^3 mesh with three scalars approximately 55 s of c.p.u. were required per evaluation and three eddy-turnover times required 70 h of Cray time.

3. Forcing, simulation parameters, and aliasing limits

The codes outlined have been used for forced and decaying simulations. This paper will concentrate on the higher-order correlations obtained when the large scales are forced. The decaying calculations are discussed in detail by Herring & Kerr (1982) and Kerr (1981), though some of those results are included here in figure 3.

Why do we force the large scales? Ideally we would like to simulate an infinite domain with unlimited resolution of the smallest scales, but in practice we are limited to a finite box with a finite mesh. There is a minimum wavenumber associated with the size of the box and a maximum wavenumber associated with the mesh spacing. If the effects of these limits are to be minimized, the energy must be restricted to a very small range of wavenumbers and the Reynolds number must be small. The calculations discussed in Herring & Kerr (1982) simulate decaying flow behind a grid and are restricted in this way.

By forcing the large scales, some of the restrictions imposed by the low-wavenumber limit can be removed. It is believed that for sufficiently large Reynolds numbers there is a cascade of energy from large to small scales which maintains a statistically steady state. By forcing we hope to mimic a cascade from wavenumbers smaller than the minimum wavenumber to those in our computational box. Forcing would also maintain a steady spectrum at moderate Reynolds numbers and allow us to collect statistics of the higher-order correlations. Since the derivative correlations are representative of the small scales or high wavenumbers, it is hoped that they will not be affected by the details of the large scales, in our case the details of the artificial forcing used. Our approach is opposite to that of many turbulence modellers, who are primarily interested in the large scales and model the small scales.

Both the velocity and scalar were forced by time-advancing the lowest-wavenumber band ($1 \leqslant k/k_0 < 2$, where k_0 is the lowest wavenumber of the code) independently of the high wavenumbers. The modes calculated in this manner were included in the full equations and the higher modes were advanced as usual. Details of the numerics may be found in Kerr (1981). Low-order systems, such as our forced-wavenumber band, are known to behave chaotically, often with an associated strange attractor. To determine whether a system is chaotic or has a complicated periodic motion requires integration over many characteristic timescales and the determination of the Lyapunov exponent. Since our calculations cover only a few characteristic times a detailed analysis is not possible, but analysis of single modes in our forced wavenumber band does suggest chaotic behaviour. Our forcing is different to that used by Siggia (1981*a*), whose forcing modes were outside his computational box. Numerical tests suggest that the exact nature of the forcing is irrelevant, so long as the energy in the first wavenumber band is constant.

We present results from 27 forced cases for the Taylor-microscale Reynolds number R_λ between 9 and 82.9 and the Prandtl number between 0.1 and 2.0 (see table 1), but will discuss only a few in detail. All but one of the simulations includes a passive scalar. The exception (labelled F12 in table 1) uses the original dealiased Superbox code and our forcing to discern the effect of aliasing.

Each simulation was run until a statistically steady state was reached, usually at about two eddy-turnover times. An eddy-turnover time is defined as

$$t_e = \frac{L}{U}, \tag{11}$$

where

$$L = \frac{3\pi}{4E} \int k^{-1} E(k)\, \mathrm{d}k \tag{12}$$

Run	Mesh	R_λ	Pr	Δt	N_f	K_k	K_{OC}	t_e
F1	32^3	9.0	2.0	19.0	20	9.4	15.8	4.7
F2	32^3	9.0	0.5	19.0	20	9.4	5.6	4.7
F3	32^3	12.3	2.0	13.6	35	11.9	20.0	3.55
F4	32^3	12.3	1.0	13.6	35	11.9	11.9	3.55
F5	32^3	12.3	0.5	13.6	35	11.9	7.8	3.55
F6	32^3	18.5	1.0	9.6	25	16.5	16.5	1.97
F7a	32^3	18.5	0.5	39.0	40	16.4	9.8	1.98
F7b	32^3	18.5	0.5	9.0	10	16.5	9.8	1.97
F8	32^3	18.5	0.1	9.6	25	16.5	2.9	1.97
F9	32^3	24.0	0.5	9.5	20	21.4	12.7	1.26
F10	32^3	24.0	0.1	9.5	20	21.4	3.8	1.26
F11	32^3	28.9	0.5	29.5	60	25.7	15.3	0.91
F12	32^3	28.9	—	29.5	60	25.8	—	0.91
F13	64^3	28.5	1.0	10.0	11	12.3	12.3	3.83
F14	64^3	28.5	0.5	10.0	11	12.3	7.3	3.83
F15	64^3	28.5	0.1	10.0	11	12.3	2.2	3.83
F16	64^3	37.5	1.0	4.5	10	16.0	16.0	2.51
F17	64^3	37.5	0.5	4.5	10	16.0	9.5	2.51
F18	64^3	37.5	0.1	4.5	10	16.0	2.8	2.51
F19	64^3	48.2	1.0	6.75	28	22.4	22.4	1.41
F20	64^3	48.2	0.5	6.75	28	22.4	13.3	1.41
F21	64^3	48.2	0.1	6.75	28	22.4	4.0	1.41
F22	64^3	55.9	1.0	4.00	17	27.2	27.2	1.05
F23	64^3	55.9	0.5	4.00	17	27.2	16.2	1.05
F24	64^3	55.9	0.1	4.00	17	27.2	4.8	1.05
F25	128^3	82.9	1.0	1.35	27	45.7	45.7	0.85
F26	128^3	82.9	0.5	1.35	27	45.7	27.2	0.85
F27	128^3	82.9	0.1	1.35	27	45.7	8.1	0.85

TABLE 1. Characteristics of forced simulations. Δt: Timespan of statistical sample. N_f: Number of files averaged.

is the integral lengthscale. After reaching a steady state, statistics were collected for at least one and a half more eddy-turnover times and the means and variances of a variety of velocity and scalar correlations were obtained by averaging. These statistics and the errors are discussed in detail in Kerr (1981) and Kerr (1983). Where possible, isotropic forms of the statistics were calculated to increase the sample size and in all cases the errors for the third- and fourth-order correlations were less than 10%.

Most earlier 32^3 spectral simulations (Orszag & Patterson 1972) have been limited to R_λ less than 30, based on considerations of the location of the peak of the three-dimensional velocity-dissipation spectrum (which is near the 'bulge' discussed in the following section for figure 1). Further restrictions come from considerations of trends in the derivative flatnesses. Generally, the derivative skewnesses (14, 15) and flatnesses (32, 39) increase, or remain constant, with increasing Reynolds number. Failure to do so indicates that small-scale truncation and aliasing errors are significant. This behaviour was observed for a 32^3 mesh at Reynolds numbers larger than 24. In order to demonstrate the magnitude of aliasing errors at this Reynolds number, table 2(*a*) gives derivative flatness factors for 32^3 and 64^3 calculations starting with identical initial conditions at $R_\lambda \approx 29$. On the 64^3 grid there are virtually no aliasing or truncation errors at this Reynolds number for any of the Prandtl numbers used. Any differences between the 32^3 and 64^3 results are due to aliasing and high-wavenumber truncation errors in the 32^3 simulation. In run F11

Run	Grid size	Pr	$F_{\partial u^4}$ (64)	$F_{\partial\theta^4}$ (64)	$F_{\partial u^4}$ (32)	$F_{\partial\theta^4}$ (32)
			(*a*) Averages of many realizations			
F11	32	0.5	—	—	3.94	5.73
F12	32	—	—	—	4.17	—
F13	64	1.0	4.18	6.88	—	—
F14	64	0.5	4.18	5.82	—	—
F15	64	0.1	4.18	3.61	—	—
			(*b*) One realization			
F13	64	1.0	3.99	7.30	3.93	5.62
F14	64	0.5	3.99	5.95	3.93	5.08
F15	64	0.1	3.99	3.55	3.93	3.57

TABLE 2. Velocity and scalar flatness factors used to determine aliasing errors. F11 is 32 cubed aliased. F12 is 32 cubed dealiased. The size of the grid used to calculate the flatnesses is in parentheses.

only spherical truncation is used to dealias; while F12 uses the original Superbox code to dealias by shifting grids on each evaluation. For F11 (aliased) both the velocity-derivative flatness and scalar-derivative flatness for $Pr = 0.5$ are significantly lower than the 64^3 results (F14), while in F12 (dealiased) there is virtually no difference with F14. Therefore, at this Reynolds number an aliased 32^3 calculation does not resolve the small scales, whereas a dealiased calculation does.

To estimate the maximum allowable Reynolds numbers on the 64^3 and 128^3 grids, the Kolmogorov wavenumber cutoffs of the simulations can be compared with the maximum wavenumbers allowed by the grids. For the inertial range ($E(k) \sim K_0 \epsilon^{\frac{2}{3}} k^{-\frac{5}{3}}$) $R_\lambda \sim K_{\mathrm{k}}^{\frac{2}{3}}$. But the Reynolds numbers in the 32^3 and 64^3 simulations are too low for an inertial range to appear and $R_\lambda \sim K_{\mathrm{k}}^{1.25}$ fits our results better. If the maximum allowable Kolmogorov wavenumber on a 64^3 grid is assumed to be twice that permitted on a 32^3 grid, then to ensure that the small scales in the 64^3 simulation are fully resolved, the maximum R_λ is $55.9 (\approx 24 \times 2^{1.25})$. As shown in figure 1, our 128^3 simulation has a noticeable $-\frac{5}{3}$ inertial range, so the $K_{\mathrm{k}}^{\frac{2}{3}}$ law should be used and $R_\lambda = 82.9 (\approx 52 \times 2^{0.67})$.

In addition to its effect on the calculation of the velocity and scalar fields, aliasing can introduce errors in the calculation of the derivative-flatness factors. To estimate this error the derivative flatnesses for a 64^3 simulation were calculated on a 32^3 grid for one realization. Table 2 (*b*) shows that the velocity-derivative flatness calculated on a 32^3 grid yields a slightly smaller result. This reinforces our conclusion that $R_\lambda \sim 29$ is slightly too high for a 32^3 grid. The scalar-derivative flatness for $Pr = 0.5$ shows aliasing errors similar to those in the velocity field, so no further restrictions on the Reynolds number are necessary when $Pr \leqslant 0.5$. On the other hand, a significant decrease is seen in the scalar-derivative flatness for $Pr = 1.0$ when it is calculated on a 32^3 grid.

Naïvely one would expect that for Prandtl number of 1, where the viscosity and scalar diffusivity are the same, there would be similar truncation effects for the velocity and the scalar. Instead, the scalar errors are much larger. What does theory tell us? For Prandtl number greater than 1, Batchelor (1959) predicts a new spectral regime in which scalar variance diminishes as k^{-1} for wavenumbers greater than the Kolmogorov wavenumber. The cutoff for the new spectral regime is $k_{\mathrm{B}} = (\epsilon/\nu D^2)^{\frac{1}{4}}$. This spectral regime has been observed (see Monin & Yaglom 1975, p. 513). Since

a higher Prandtl number implies a higher spectral cutoff, for large Prandtl numbers truncation effects will appear even at very low Reynolds numbers. Consequently for $Pr = 2$, $R_\lambda > 12$ was not run on a 32^3 mesh. But an anomalous k^{-1} subrange is also observed experimentally for Prandtl number as low as 0.7, the atmospheric value (the 'bump', Hill 1978). Therefore, even at $Pr = 1$ truncation, as indicated by the scalar-derivative flatness, becomes important for $R_\lambda > 18$ on a 32^3 grid.

Because of these difficulties our simulations are restricted to low Prandtl numbers. Some of the simulations for $Pr = 1$ are included in the plots of the correlations, but only for lower Reynolds numbers. Prandtl numbers of current experimental interest that we can simulate are 0.7, the atmospheric value, and moderately low Prandtl numbers, such as found in liquid metals. Extremely low values cannot be simulated satisfactorily because the relevant low-wavenumber cutoff is the Oboukov–Corrsin cutoff, K_{OC} (10*b*), and this would be below the minimum wavenumber of the simulation. The lowest value we use is $Pr = 0.1$. Analysis of spectra in §4 support these conclusions.

4. Spectra and skewnesses

Since most simulators determine whether there is significant truncation error by inspecting high-wavenumber spectra, we have included some spectra to demonstrate the validity of our method. Figure 1 shows three-dimensional energy spectra, normalized by the Kolmogorov microscales and multiplied by $k^{\frac{5}{3}}$, for several Reynolds numbers. The turnup at large wavenumbers is a numerical effect of the large-wavenumber cutoff. Where the turnup is small, the small scales are well resolved. The turnup for $R_\lambda = 55.9$ in a 64^3 simulation and $R_\lambda = 82.9$ in the 128^3 simulation is the most we could accept. The three-dimensional kinetic-energy and scalar-variance spectra for our largest Reynolds number, 82.9, are plotted in figure 2. The velocity spectrum is normalized as in figure 1 and the scalar spectra are normalized by the Kolmogorov microscales and the scalar-variance dissipation in a similar manner. When compared with the scalar variance at low wavenumbers, the turnup at high wavenumbers for $Pr = 1$ is unacceptably large. This reinforces our conclusion that moderate to high Prandtl numbers can be simulated only with low-Reynolds-number simulations.

With the exception of deviations in the lowest Reynolds-number spectrum ($R_\lambda = 18.5$), all of the spectra in figure 1 collapse to a single curve in the dissipation range. In addition, a short $-\frac{5}{3}$ regime appears in the 128^3 spectrum ($R_\lambda = 82.9$) at low wavenumbers. For comparison, the dashed line in figure 1 fits a spectrum of the form predicted by Pao (1965),

$$E(k) = K_0 \epsilon^{\frac{2}{3}} k^{-\frac{5}{3}} \exp\left(-1.5 K_0 \nu \epsilon^{-\frac{1}{3}} k^{\frac{4}{3}}\right), \tag{13}$$

to the computed spectra with K_0, the Kolmogorov constant, equal to 2.45. Although experimental values for the Kolmogorov constant as high as 2.1 have been reported (Gibson, Stegen & Williams 1970), the fitted value is much higher than the usual experimental value of 1.4 to 1.7 (Monin & Yaglom 1975, pp. 483–485). Pao's spectral form is used because it provides a means of comparing three-dimensional spectra from simulations with experimental one-dimensional spectra. For example, experimental spectra in Champagne *et al.* (1977) show a high-wavenumber bulge when compared with Pao's form and there are similar differences between the calculated spectra of figure 1 and Pao's form near $(\eta k) \sim 0.2$. Our simulation would be consistent with the experiments (that is $K_0 \sim 1.7$) if a higher Reynolds number simulation gave the

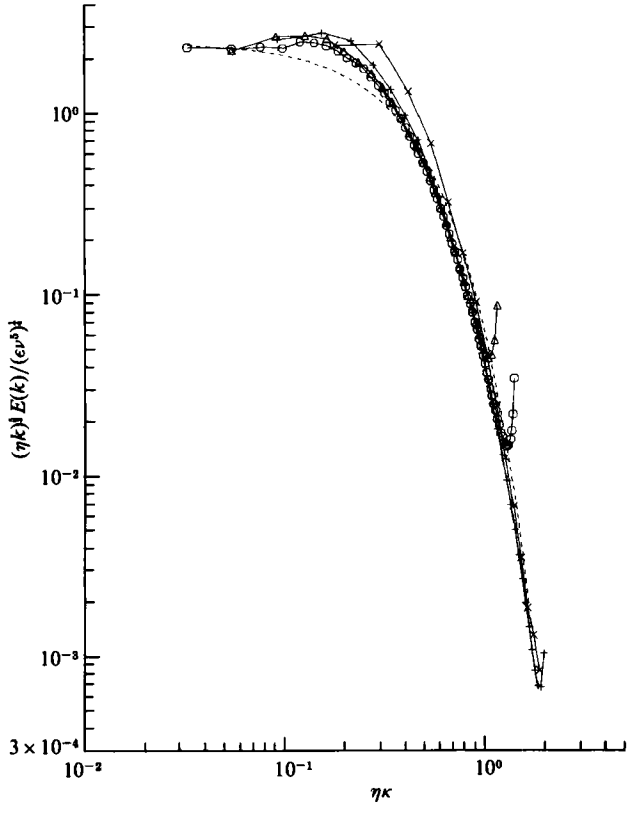

FIGURE 1. Kinetic-energy spectra normalized by the Kolmogorov microscales (10*a*) and multiplied by $k^{\frac{5}{3}}$: Pao's theoretical curve (13) for $K_0 = 2.45$ is indicated by (---). ○, $R_\lambda = 82.9$; △, $R_\lambda = 55.9$; +, $R_\lambda = 37.2$; ×, $R_\lambda = 18.4$.

correct Kolmogorov constant in the inertial range. This conclusion is supported by analysis of the velocity-derivative skewness.

For both the velocity and scalar three classes of the derivative skewnesses can be defined. These are the real-space derivative skewnesses, spectral-transfer skewnesses, and dissipation skewnesses. The real-space derivative skewnesses are measurable with hot-wire probes. The spectral and dissipation skewnesses are not strictly third-order moments, but in isotropic flow they are related to the real-space derivative skewnesses. The measurable real-space derivative skewnesses are the velocity-derivative skewness,

$$S_u = \frac{\left\langle \left(\frac{\partial u_1}{\partial x_1}\right)^3 \right\rangle}{\left\langle \left(\frac{\partial u_1}{\partial x_1}\right)^2 \right\rangle^{\frac{3}{2}}}, \tag{14}$$

which equals $F_{\partial u^3}$ (3), the mixed-derivative skewness

$$S_{u\theta} = \frac{\left\langle \left(\frac{\partial u_1}{\partial x_1}\right)\left(\frac{\partial \theta}{\partial x_1}\right)^2 \right\rangle}{\left\langle \left(\frac{\partial u_1}{\partial x_1}\right)^2 \right\rangle^{\frac{1}{2}} \left\langle \left(\frac{\partial \theta}{\partial x_1}\right)^2 \right\rangle}, \tag{15}$$

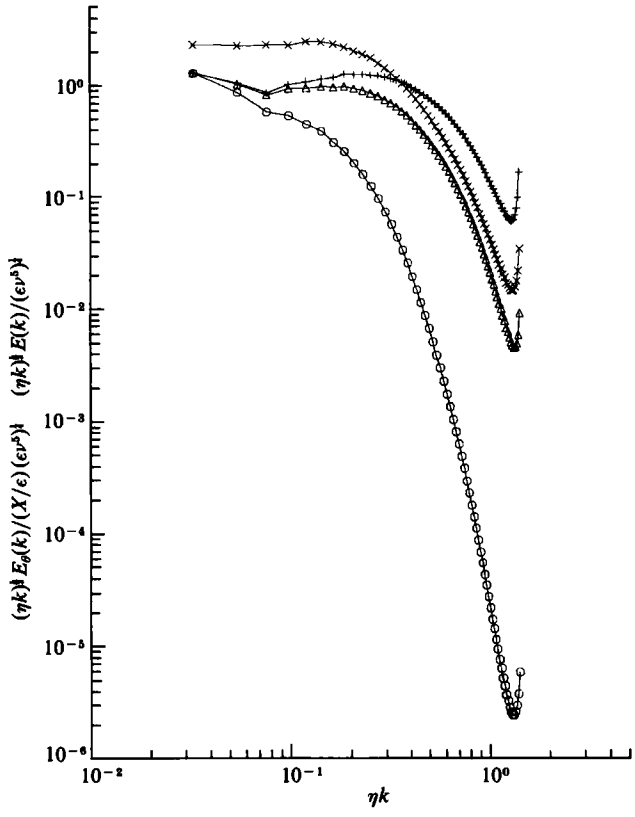

FIGURE 2. Kinetic-energy and passive-scalar spectra at $R_\lambda = 82.9$ normalized by the Kolmogorov microscales (10*a*) and the scalar-variance dissipation, χ. ○, $Pr = 0.1$; △, $Pr = 0.5$; +, $Pr = 1.0$; ×, kinetic energy.

and the scalar-derivative skewness

$$S_\theta = \frac{\left\langle \left(\frac{\partial \theta}{\partial x_1}\right)^3 \right\rangle}{\left\langle \left(\frac{\partial \theta}{\partial x_1}\right)^2 \right\rangle^{\frac{3}{2}}}. \tag{16}$$

In isotropic turbulence the terms in the velocity-derivative skewness and the mixed-derivative skewness can be written more generally. That is,

$$\frac{35}{2}\left\langle \left(\frac{\partial u_1}{\partial x_1}\right)^3 \right\rangle = \tfrac{4}{3}\langle \mathrm{tr}\, e^3 \rangle \tag{17a}$$

$$= -\langle \omega_i e_{ij} \omega_j \rangle \tag{17b}$$

(Betchov 1956) and

$$\frac{15}{2}\left\langle \frac{\partial u_1}{\partial x_1}\left(\frac{\partial \theta}{\partial x_1}\right)^2 \right\rangle = \langle \theta_i e_{ij} \theta_j \rangle. \tag{18}$$

Furthermore,

$$\left\langle \left(\frac{\partial u_1}{\partial x_1}\right)^2 \right\rangle = \frac{\frac{1}{15}\epsilon}{\nu} \tag{19a}$$

and $$\left\langle \left(\frac{\partial\theta}{\partial x_1}\right)^2 \right\rangle = \frac{\chi}{6D}. \tag{19b}$$

These rotationally invariant forms are used in all our calculations of the real-space skewnesses.

The spectral-transfer skewnesses and the dissipation skewnesses are related to the real-space skewnesses through integral equations for the dissipation of energy and scalar variance,

$$\frac{1}{2\nu}\frac{\mathrm{d}}{\mathrm{d}t}\epsilon = \int k^2 T_u(k)\,\mathrm{d}k - 2\nu\int k^4 E_u(k)\,\mathrm{d}k \tag{20}$$

and

$$\frac{1}{2D}\frac{\mathrm{d}}{\mathrm{d}t}\chi = \int k^2 T_\theta(k)\,\mathrm{d}k - D\int k^4 E_\theta(k)\,\mathrm{d}k, \tag{21}$$

where $T_u(k)$ and $T_\theta(k)$ are the nonlinear energy and scalar-variance transfers, respectively. For our forced equations another term should be added, but this term is negligible except at low Reynolds numbers. The second-order moments of the transfers are related to the real-space skewnesses by

$$\int k^2 T_u(k)\,\mathrm{d}k = \langle \omega_i e_{ij} \omega_j \rangle \quad \text{and} \quad \int k^2 T_\theta(k)\,\mathrm{d}k = -\langle \theta_i e_{ij} \theta_j \rangle,$$

identically. The integrals of the transfers are zero ($\int T(k)\,\mathrm{d}k = 0$), but because there is a net cascade of kinetic energy and scalar variance to higher wavenumbers, their second-order moments will in general be positive and non-zero. Therefore, we can define two spectral-transfer skewnesses, the velocity spectral skewness

$$S_{u(k)} = \frac{2}{35}\frac{\int k^2 T_u(k)\,\mathrm{d}k}{(\epsilon/15\nu)^{\frac{3}{2}}} = \frac{2}{35}\frac{P_\Omega}{(\epsilon/15\nu)^{\frac{3}{2}}}, \tag{22}$$

and the mixed spectral skewness

$$S_{\theta(k)} = \frac{2}{15}\frac{\int k^2 T_\theta(k)\,\mathrm{d}k}{(\epsilon/15\nu)^{\frac{1}{2}}(\chi/6D)}, \tag{23}$$

where P_Ω is the rate of enstrophy production and Ω, the enstrophy, equal to $\frac{1}{2}\langle \omega_i \omega_i \rangle$. Because the spectral-transfer skewnesses are non-zero, in isotropic flow the velocity- and mixed-derivative skewnesses will also be non-zero and obey

$$S_u = -S_{u(k)}, \quad S_{u\theta} = -S_{\theta(k)}.$$

These arguments do not apply to the real-space scalar-derivative skewness (16), which is zero in an isotropic calculation such as ours. However, it has recently been found that, in shear flows with a temperature gradient, the scalar-derivative skewness is non-zero (Sreenivasan & Tavoularis 1980).

For our statistically steady forced simulations $\mathrm{d}\epsilon/\mathrm{d}t \to 0$ and $\mathrm{d}\chi/\mathrm{d}t \to 0$, so we expect that, as the Reynolds numbers increase,

$$\int k^2 T_u \to 2\nu \int k^4 E_u \quad \text{and} \quad \int k^2 T_\theta \to D \int k^4 E_\theta.$$

Therefore, a third measure of the skewnesses, the dissipation skewnesses, can be defined by (Wyngaard & Tennekes 1970 and Wyngaard 1971)

$$S_\epsilon = \frac{2}{35}\frac{\epsilon_\Omega}{(\epsilon/15\nu)^{\frac{3}{2}}}, \tag{24}$$

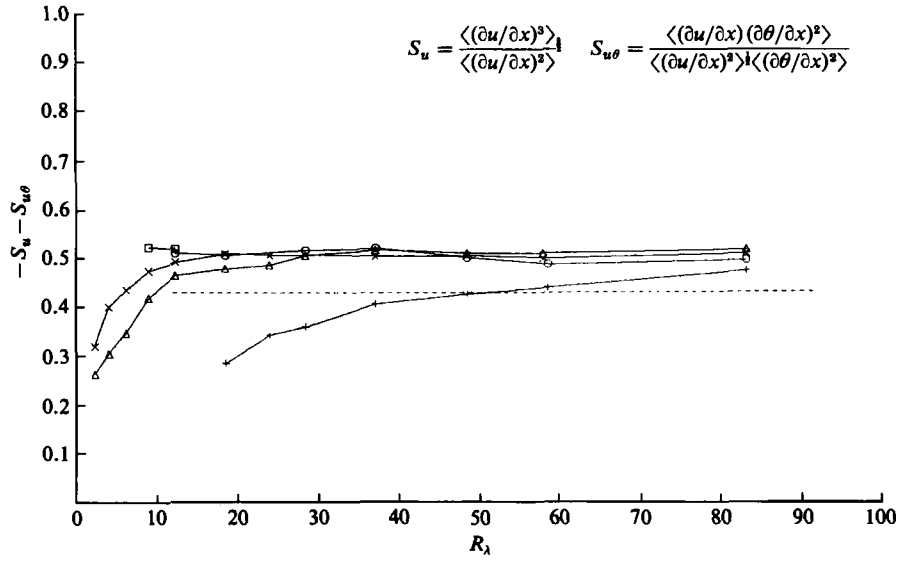

FIGURE 3. Dependence of the velocity-derivative skewness (14) and mixed-derivative skewness (15) on Taylor-microscale Reynolds number: (---) is the experimental data of Klebanoff (private communication) where $S_u = 0.43$; □, $Pr = 2.0$; ○, $Pr = 1.0$; △, $Pr = 0.5$; +, $Pr = 0.1$; ×, velocity.

and
$$S_\chi = \tfrac{2}{15} D \frac{\int k^4 E_\theta(k)\,\mathrm{d}k}{(\epsilon/15\nu)^{\frac{1}{2}}(\chi/6D)}, \tag{25}$$

where
$$\epsilon_\Omega = -\frac{\mathrm{d}\Omega}{\mathrm{d}t} = 2\nu \int k^4 E(k)\,\mathrm{d}k \tag{26}$$

is the enstrophy dissipation rate.

As discussed in §1, all the higher-order correlations are expected to deviate from their uncorrelated values as the Reynolds number increases. Experimentally, the velocity-derivative skewness increases from zero, the uncorrelated value, to a value greater than 0.3 at very low experimental Reynolds numbers and appears to increase indefinitely in very high Reynolds-number atmospheric measurements (Tavoularis, Bennett & Corrsin 1978). But at intermediate Reynolds numbers the experiments are less conclusive. Tavoularis *et al.* (1978) cite data which suggests that the skewness decreases with Reynolds number between $R_\lambda = 10$ and 500. P. S. Klebanoff (National Bureau of Standards, private communication, 1982) finds the velocity-derivative skewness to be constant and equal to 0.43 between $R_\lambda = 40$ and 200 in a boundary layer. This experimental result is plotted in figure 3.

Simulations discussed in Herring & Kerr (1982) show that the velocity-derivative skewness increases from 0 to 0.4 by $R_\lambda \sim 20$, in agreement with low-Reynolds-number experiments. They find that the mixed-derivative skewness increases in a similar manner. At intermediate Reynolds numbers, they suggest that both the velocity- and mixed-derivative skewnesses reach maximum values, then remain constant with increasing Reynolds number, agreeing with Klebanoff's experiment. With our 64^3 and 128^3 simulations we have determined the skewnesses at higher Reynolds numbers and confirmed those results (figure 3). Figures 3 and 4 plot the real-space and dissipation skewnesses, respectively, as functions of R_λ, and in all cases the magnitudes of the

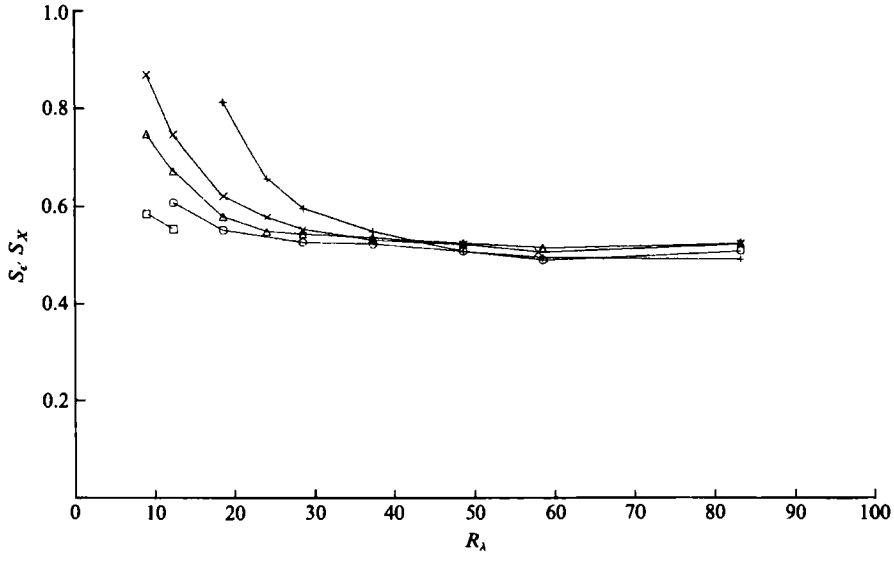

FIGURE 4. Dependence of the velocity-dissipation skewness (24) and the scalar-dissipation skewness (25) on Taylor-microscale Reynolds number. For symbols see figure 3.

skewnesses converge to approximately 0.5. The value for the velocity-derivative skewness for simulations F11 to F27 is -0.505 ± 0.005.

The statistical models of the small scales and the atmospheric measurements mentioned predict that the velocity-derivative skewness will increase very slowly with Reynolds number (4, 5). Although the accuracy of our curve is not good enough to rule out the existence of such a trend, it appears significant that both our simulation and some experiments show no Reynolds-number dependence over a wide range. The reason the velocity-derivative skewness does not increase with Reynolds number is probably related to the alignment of small-scale structures. Recall that the model of Tennekes (1968) suggested that if the structures are tubes, then the skewness would not increase with Reynolds number. In §7 (Graphics) it will be seen that our structures are tubes. In addition, fourth-order statistics and our graphics find strong alignment between the vorticity and the rate of strain.

Because of the connection between the velocity skewnesses and the fourth-order moment of the spectra, a simple relation between the velocity-derivative skewness and the Kolmogorov constant exists. If Pao's spectral form (13) is used with the equation for the velocity-dissipation skewness (24),

$$S_u = -2.40 K_0^{-\frac{3}{2}}. \tag{27}$$

For $S_u = -0.5$, $K_0 = 2.85$. For a typical experimental Kolmogorov constant, $K_0 = 1.7$, (27) gives $S_u = -1.08$, which disagrees with experimental measurements of the skewness at moderate Reynolds numbers. Therefore, the experimental skewness and our calculated spectra (figure 1) suggest that, in the wavenumber range calculated, the effective Kolmogorov constant is large. Because the major contribution to the skewness comes from the wavenumber regime we have simulated, this could be consistent with a much lower Kolmogorov constant in the inertial range. It is consistent with the high-wavenumber bulge seen in the experimental spectra of Champagne *et al.* (1977). Additional experiments which determine both the Kolmogorov constant and the skewness would help answer these questions.

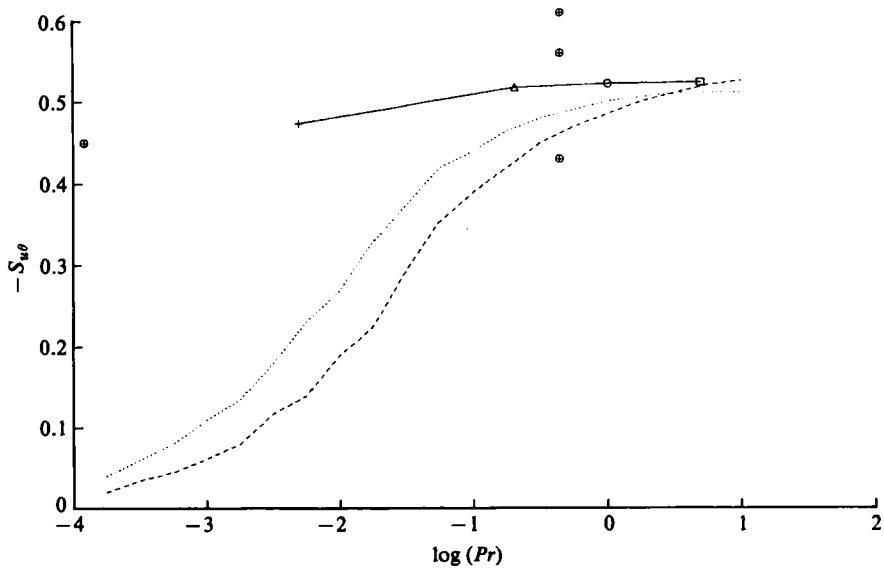

FIGURE 5. Dependence of the mixed-derivative skewness (15) on Prandtl number: Test field model results (– – –), the model of Hill (1978) (·····), and experiments (⊕) are all taken from Larcheveque *et al.* (1980). Symbols for our simulations (——) are the same as in figure 3.

There are no experiments or phenomenological models with which to compare our results on the dependence of the mixed-derivative skewness with Reynolds numbers. But there are arguments that the mixed-derivative skewness should increase with Prandtl number, possibly with an upper bound at a high Prandtl number for given Reynolds number (Hill 1978). Hill's arguments assume that there are two spectral regimes for the scalar variance at low Prandtl numbers, a $k^{-\frac{5}{3}}$ inertial regime and a $k^{-\frac{17}{3}}$ inertial–diffusive regime. There are strong theoretical arguments in favour of both spectral regimes (Corrsin 1951 and Batchelor, Howells & Townsend 1959). Experimentally, a $k^{-\frac{5}{3}}$ inertial range for the scalar variance has been well demonstrated (Monin & Yaglom 1975, p. 511), but the evidence for a $k^{-\frac{17}{3}}$ inertial-diffusive regime is tenuous. This is due in part to the exotic nature of low-Prandtl-number materials, such as liquid mercury and sodium. Experimental results on the dependence of the mixed-derivative skewness on Prandtl number are also difficult to obtain. With the exception of a few measurements in air ($Pr = 0.7$ in figure 4) the only measurements of the mixed-derivative skewness were taken in water and liquid mercury by Clay (1973). For air, measurements in the atmosphere (Antonia & Van Atta 1978) give much larger values than those in wind tunnels. Our results, Hill's model 4, the test field model (Larcheveque *et al.* 1980), and several experimental values (taken from Larcheveque *et al.*) are shown in figure 5. Our values are the maximum $S_{u\theta}$ for a given Prandtl number in our simulations (see figure 3). The experiments of Clay (1973) suggest that there is virtually no dependence on Prandtl number, which is compatible with our results. Figure 3 suggests that for higher Reynolds numbers $S_{u\theta}$ will asymptote to -0.5 for $Pr = 0.1$, but remain constant for $Pr = 0.5$ and 1.0. In this case, simulations at higher Reynolds numbers should show that the mixed-derivative skewness is constant over a wide range of Prandtl numbers. A long crossover regime between the $k^{-\frac{5}{3}}$ and $k^{-\frac{17}{3}}$ spectral ranges could explain this result. Gibson (1968) has suggested that this new regime should go as k^{-3}, but the spectrum for $Pr = 0.1$ in figure 2 does not support this.

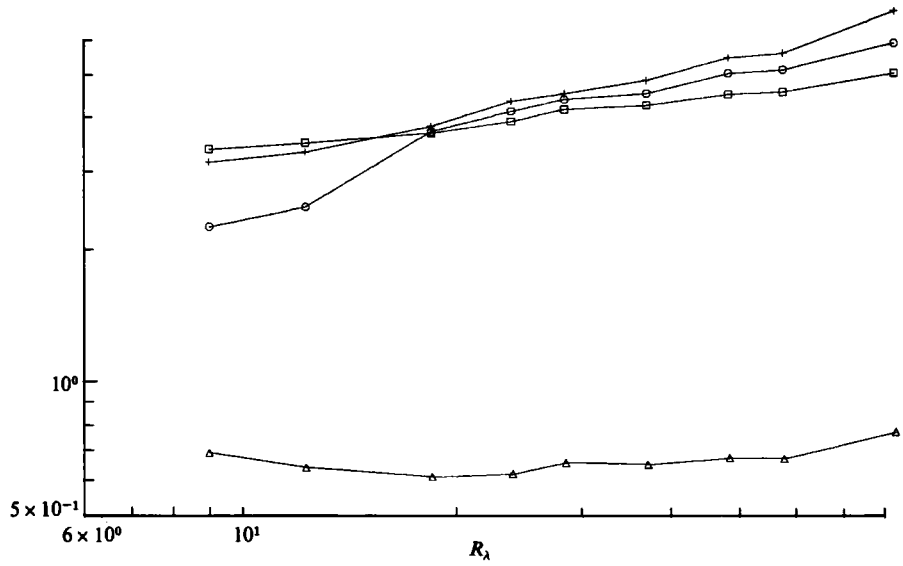

FIGURE 6. Dependence of the rotationally invariant fourth-order velocity-derivative correlations on Taylor-microscale Reynolds number: □, F_1 (32) or the velocity-derivative flatness; $F_{\partial u^4}$ (3); ○, F_2 (33); △, F_3 (34); +, F_4 or the vorticity flatness, F_{ω^4} (38).

5. Fourth- and higher-order velocity correlations

Siggia (1981*b*) has shown that in isotropic flow all fourth-order velocity-derivative correlations can be expressed in terms of four rotational invariants of the velocity-deformation tensor. These are

$$I_1 = \langle e^4 \rangle, \quad I_2 = \langle \omega^2 e^2 \rangle, \tag{28), (29}$$

$$I_3 = \langle \omega_i e_{ij} e_{jk} \omega_k \rangle \quad \text{and} \quad I_4 = \langle \omega^4 \rangle, \tag{30), (31}$$

where

$$e_{ij} = \tfrac{1}{2}[(\partial u_i/\partial x_j) + \partial u_j/\partial x_i)]$$

is the rate of strain, $e^2 = \Sigma e_{ij}^2$, $e^4 = (e^2)^2$, $\omega_i = (\nabla \times \boldsymbol{u})_i$ is the vorticity, and $\omega^2 = \Sigma \omega_i^2$. We will normalize these correlations as follows:

$$F_1 = \frac{15}{7} \frac{I_1}{\langle e^2 \rangle^2}, \quad F_2 = 3 \frac{I_2}{\langle \omega^2 \rangle \langle e^2 \rangle}, \tag{32), (33}$$

$$F_3 = 3 \frac{I_3}{\langle \omega^2 \rangle \langle e^2 \rangle} \quad \text{and} \quad F_4 = \frac{9}{5} \frac{I_4}{\langle \omega^2 \rangle^2}. \tag{34), (35}$$

Their uncorrelated values are 3, 3, 1 and 3 respectively, and they are plotted in figure 6. The only fourth-order velocity-derivative correlation that has been experimentally determined is the velocity-derivative flatness, $F_{\partial u^4}$ (3), which equals F_1 if isotropy is assumed. We have normalized (32), (33), and (35) to 3 for comparison with $F_{\partial u^4}$, whose Gaussian value is 3, and estimated scaling exponents for these correlations. Unlike the other fourth-order correlations, F_3 (34) can be its uncorrelated value even without Gaussian statistics, and so it has been normalized to 1.

Kuo & Corrsin (1971) find that $F_{\partial u^4}$ increases with Reynolds number as $R_\lambda^{\alpha_4}$ with $\alpha_4 = 0.25$ for $12 < R_\lambda < 100$. Our flatness (F_1 or $F_{\partial u^4}$, figures 6, 7 and 8) also increases

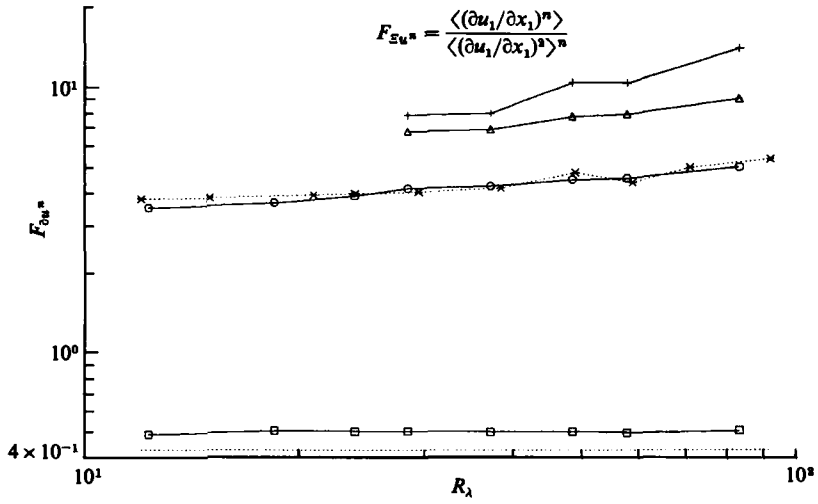

FIGURE 7. Dependence of the velocity-derivative correlations, $F_{\partial u^n}$ (3) on Taylor-microscale Reynolds number: □, third order, or the velocity-derivative skewness, S_u (14); ○, fourth order, the velocity-derivative flatness or F_1 (32); △, fifth order; +, sixth order, which has been divided by 5 so it will appear on this graph; (·····), experimental data of Klebanoff (private communication) for the velocity-derivative skewness and * the velocity-derivative flatness.

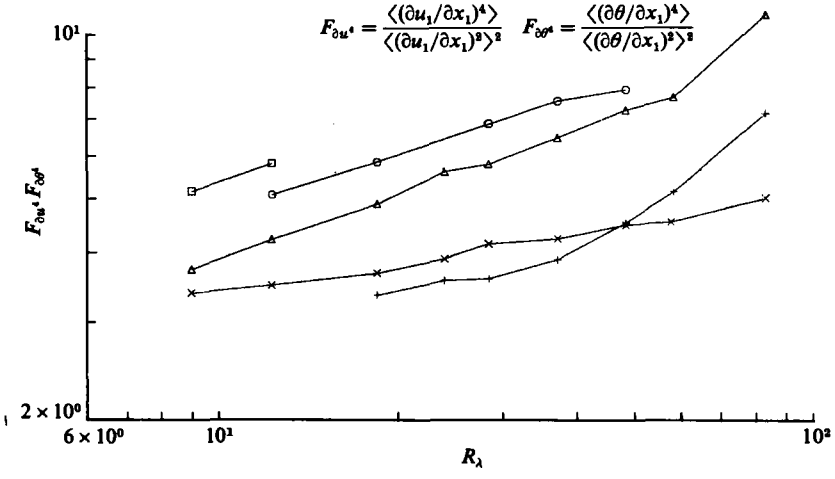

FIGURE 8. Dependence of the velocity-derivative flatness (3, 32) and the scalar-derivative flatness (39, 41) on Taylor-microscale Reynolds number. The experiment of Sreenivasan *et al.* (1980) is a *. For the remaining symbols see figure 3.

with Reynolds number and is in excellent agreement with the experiment of Frenkiel & Klebanoff (1975) (upper dotted line, figure 7), but $\alpha_4 = 0.18 \pm 0.03$.

If only one scaling exponent is necessary to describe intermittency (as suggested by the phenomenological models), all the fourth-order velocity-derivative correlations should exhibit similar behaviour. If power laws are fitted to F_1, F_2, and F_4 for R_λ greater than 28, the exponents are 0.18 ± 0.03, 0.29 ± 0.03 and 0.37 ± 0.03, respectively. This suggests that not one, but at least two scaling exponents are necessary, one for the rate of strain and the other for the vorticity. Furthermore, F_3 decreases noticeably

with Reynolds number at very low Reynolds number and rises only a small amount at higher Reynolds numbers. The low value for F_3 suggests that the principal component of the rate of strain and the vorticity tend to be perpendicular to each other, which would always be the case in two dimensions, and implies that there is strong alignment in the small-scale turbulent structures. This is demonstrated by the graphics discussed in §7. The similarity between one of the isotropic forms of the skewness (17*b*) and I_3 suggests that the low value for F_3 is related to the invariance of the velocity-derivative skewness.

Although the computed fourth-order correlations suggest that several scaling exponents are necessary, it is possible that at much higher Reynolds numbers one scaling exponent is sufficient. If so, the self-similar regime described by the models has not been reached. The slight rise in F_3 might indicate that the calculations are approaching this regime. A change in the velocity-derivative flatness scaling exponent at higher Reynolds numbers would be seen as all the exponents approach the asymptotic value. This could be interpreted as a variation in the dissipation–dissipation correlation exponent μ with Reynolds number. Experimentally, the Reynolds-number dependence of the velocity-derivative skewness and flatness is different at very high Reynolds number, with $\alpha_4 \sim 0.32$ for $R_\lambda = 200$ to 20000 (Van Atta & Antonia 1980). There are two experimental measurements that would help clarify this matter. If u_2 and u_1 can be measured simultaneously, which now seems possible with crossed-wire probes, then

$$I_5 = \left\langle \left(\frac{\partial u_1}{\partial x_1}\right)^2 \left(\frac{\partial u_2}{\partial x_1}\right)^2 \right\rangle = \frac{I_1}{105} + \frac{I_2}{70} - \frac{I_3}{105} \tag{36}$$

and

$$I_6 = \left\langle \left(\frac{\partial u_2}{\partial x_1}\right)^4 \right\rangle = \tfrac{3}{140} I_1 + \tfrac{11}{140} I_2 - \tfrac{3}{35} I_3 + \tfrac{1}{80} I_4 \tag{37}$$

could be measured. If the trends calculated are correct, I_2 should dominate in I_5, and I_4 should dominate in I_6. This implies that the scaling exponent of the normalized correlation of I_5 should be greater than that of $F_{\partial u^4}$, and the scaling exponent of the normalized correlation of I_6 should be the largest.

The fifth–eighth-order velocity-derivative correlations (3) and vorticity moments,

$$F_{\omega^n} = \frac{\langle \omega_1^n \rangle}{\langle \omega_1^2 \rangle^{\frac{1}{2}n}}, \tag{38}$$

have also been calculated. Since the statistics deteriorate as the order of the correlations increases (Kerr 1983), only the velocity-derivative skewness, flatness, and fifth- and sixth-order correlations are plotted in figure 7, even though the fifth- and sixth-order statistics are questionable. The exponents for the velocity-derivative correlations in figure 7 are 0.18 ± 0.03, 0.27 ± 0.03 and 0.55 ± 0.03 respectively. The lognormal theory predicts that these exponents should be proportional to $n(n-1)$ (equation 4) and the β-model predicts $n-2$ (equation 5). The lognormal theory provides a better fit, as in the experiments (Antonia *et al.* 1982). The associated value of the dissipation–dissipation correlation exponent μ has not been calculated because the simulations are not in the Reynolds-number regime where the experimental value is usually found.

Assuming isotropy, $F_{\omega^4} = F_4$. The most important point that can be made about the sixth-order vorticity correlation (F_{ω^6}, figure 9) is that its scaling exponent (1.1 ± 0.1) is much larger than the corresponding sixth-order velocity-derivative scaling exponent, just as was true for the fourth-order correlations.

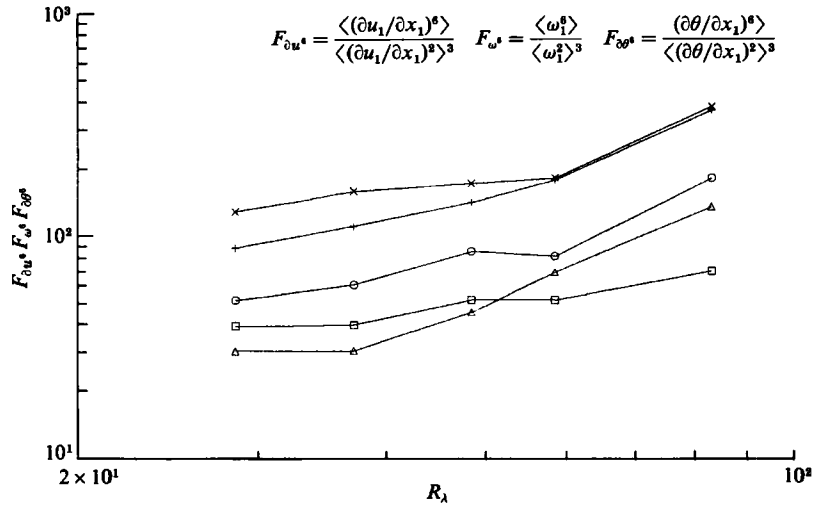

FIGURE 9. Dependence of the sixth-order velocity-derivative correlation, vorticity correlation, and scalar-derivative correlations on Taylor-microscale Reynolds number: □, the velocity, $F_{\partial u^6}$ (3); ○, the vorticity, F_{ω^6} (38); △, the scalar-derivative correlation, $F_{\partial\theta^6}$ (39), for $Pr = 0.1$; +, for $Pr = 0.5$; ×, for $Pr = 1.0$.

6. Scalar and mixed scalar–velocity fourth-order derivative correlations

There are three fourth-order derivative correlations which have been measured experimentally, the velocity-derivative flatness, $F_{\partial u^4}$ (3), the scalar-derivative flatness

$$F_{\partial\theta^n} = \frac{\left\langle\left(\dfrac{\partial\theta}{\partial x_1}\right)^n\right\rangle}{\left\langle\left(\dfrac{\partial\theta}{\partial x_1}\right)^2\right\rangle^{\frac{1}{2}n}}, \quad n = 4, \tag{39}$$

and the mixed-derivative correlation

$$F_{u\theta} = \frac{\left\langle\left(\dfrac{\partial u_1}{\partial x_1}\right)^2\left(\dfrac{\partial\theta}{\partial x_1}\right)^2\right\rangle}{\left\langle\left(\dfrac{\partial u_1}{\partial x_1}\right)^2\right\rangle\left\langle\left(\dfrac{\partial\theta}{\partial x_1}\right)^2\right\rangle}. \tag{40}$$

The uncorrelated value for the velocity- and scalar-derivative flatnesses, assuming Gaussian statistics, is 3, and the uncorrelated value for the mixed-derivative correlation is 1. The rotationally invariant form of the scalar-derivative flatness in isotropic flow is

$$F_{\partial\theta^4} = F_{\nabla\theta} = \frac{9}{5}\frac{\langle\nabla\theta^4\rangle}{\langle\nabla\theta^2\rangle^2}. \tag{41}$$

In the experiment of Antonia & Chambers (1980), the atmospheric temperature-derivative flatness increases much faster with Reynolds number than the velocity-derivative flatness. Specifically, if $F_{\partial\theta^4} \sim R_\lambda^{\alpha_\theta}$, then $\alpha_\theta = 0.5$ for $100 < R_\lambda < 10000$. In our simulations (figure 8), the scalar-derivative flatness also has a stronger dependence on Reynolds number than the velocity-derivative flatness. In addition, the scalar-derivative flatness increases with Prandtl number for given Reynolds number, while the scaling exponents decrease. For Prandtl numbers 0.1, 0.5, and 1.0 we found

$\alpha_\theta = 0.48$, 0.44 and 0.36. The trend for the flatness factors at low Prandtl numbers to increase faster with Reynolds number than at larger Prandtl numbers suggests that the large exponents for $Pr = 0.1$ and 0.5 might be transient, and that at higher Reynolds numbers they will have an exponent similiar to that for $Pr = 1.0$. That is, $\alpha_\theta = 0.36$, which is the same order as the exponent for the vorticity flatness (F_4), might be an upper bound for the scaling exponent at large Reynolds numbers for all Prandtl numbers.

Although the scalar-derivative flatness increases with R_λ at similar rates in experiment and in our simulations, the Reynolds numbers are very different. Sreenivasan *et al.* (1980) have measured the scalar-derivative flatness in a wind tunnel with temperature fluctuations produced by a heated screen and find $F_{\partial\theta^4} = 5.5$. The Prandtl number is 0.7 and, we believe, $R_\lambda \approx 24$. (R_λ was computed from their u^2 data and is consistent with similar wind-tunnel experiments by Warhaft & Lumley (1978).) For $R_\lambda \approx 24$, their result is consistent with our calculations and lies on our curve for $Pr = 0.5$ in figure 8.

The sixth-order scalar-derivative correlations $F_{\partial\theta^6}$ are plotted in figure 9. The scaling exponents for Prandtl numbers 0.1, 0.5 and 1.0 are 1.48, 1.30 and 0.92 respectively, showing the same trends with Prandtl number as the fourth-order correlations.

Before discussing the one experimentally measurable mixed correlation we will consider some rotationally invariant correlations between the velocity and scalar derivatives where both are second order. These are

$$F_{\nabla\theta\omega 1} = \frac{\langle (\nabla\theta)^2 \omega^2 \rangle}{\langle \nabla\theta^2 \rangle \langle \omega^2 \rangle}, \quad F_{\nabla\theta\omega 2} = 3\,\frac{\langle (\nabla\theta \cdot \omega)^2 \rangle}{\langle \nabla\theta^2 \rangle \langle \omega^3 \rangle}, \tag{42), (43}$$

$$F_{\nabla\theta e 1} = \frac{\langle (\nabla\theta)^2 e^2 \rangle}{\langle \nabla\theta^2 \rangle \langle e^2 \rangle} \quad \text{and} \quad F_{\nabla\theta e 2} = \frac{3 \left\langle \dfrac{\partial\theta}{\partial x_i} e_{ij} e_{jk} \dfrac{\partial\theta}{\partial x_k} \right\rangle}{\langle \nabla\theta^2 \rangle \langle e^2 \rangle}. \tag{44), (45}$$

They have been normalized so that their uncorrelated values are 1. Correlation $F_{\nabla\theta\omega 1}$ is plotted in figure 10, and is nearly 1, showing that there is little correlation between the magnitudes of the vorticity and scalar derivative. Correlation $F_{\nabla\theta\omega 2}$ is plotted in figure 11 and shows a strong anticorrelation between the direction of vorticity and the direction of the scalar gradient, which would be consistent with the scalar being wound around vortex tubes. Batchelor (1952) predicts this result for the stretching of a volume element of fluid.

Both correlations between the strain rate and the scalar derivative are greater than one and show a tendency to increase with Reynolds number for $R_\lambda < 30$, then remain constant or increase slowly, much as the skewnesses do. The experimentally measurable mixed correlation is related to $F_{\nabla\theta e 1}$ and $F_{\nabla\theta e 2}$ by

$$F_{u\theta} = \frac{\left\langle \left(\dfrac{\partial u_1}{\partial x_1}\right)^2 \left(\dfrac{\partial\theta}{\partial x_1}\right)^2 \right\rangle}{\left\langle \left(\dfrac{\partial u_1}{\partial x_1}\right)^2 \right\rangle \left\langle \left(\dfrac{\partial\theta}{\partial x_1}\right)^2 \right\rangle} = \tfrac{3}{7} F_{\nabla\theta e 1} + \tfrac{4}{7} F_{\nabla\theta e 2}, \tag{46}$$

and is plotted in figure 12. Correlation $F_{u\theta}$ has been measured by Park (1976) and is greater than one.

We have calculated a wide assortment of other correlation factors, none of which

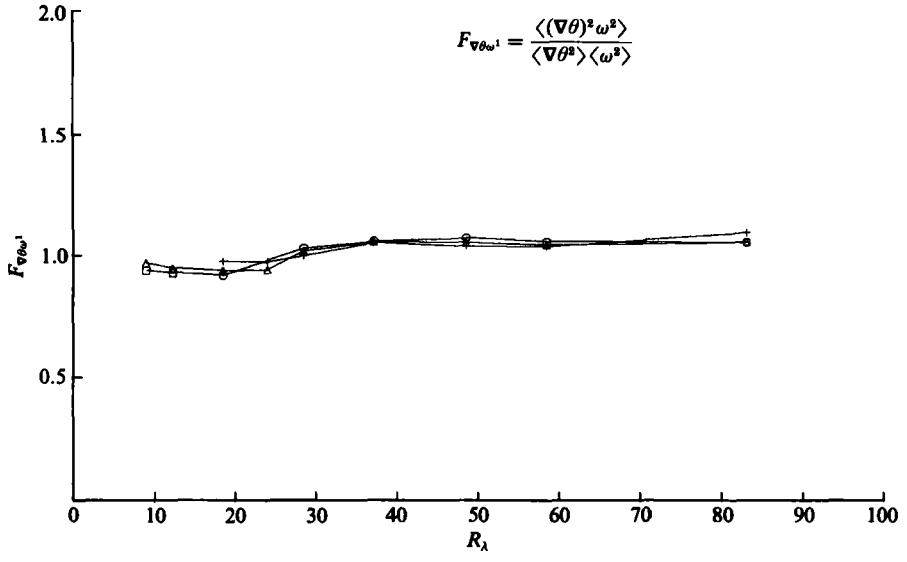

FIGURE 10. Dependence of the first scalar derivative/vorticity correlation, $F_{\nabla\theta\omega 1}$ (42), on Taylor-microscale Reynolds number. For symbols see figure 3.

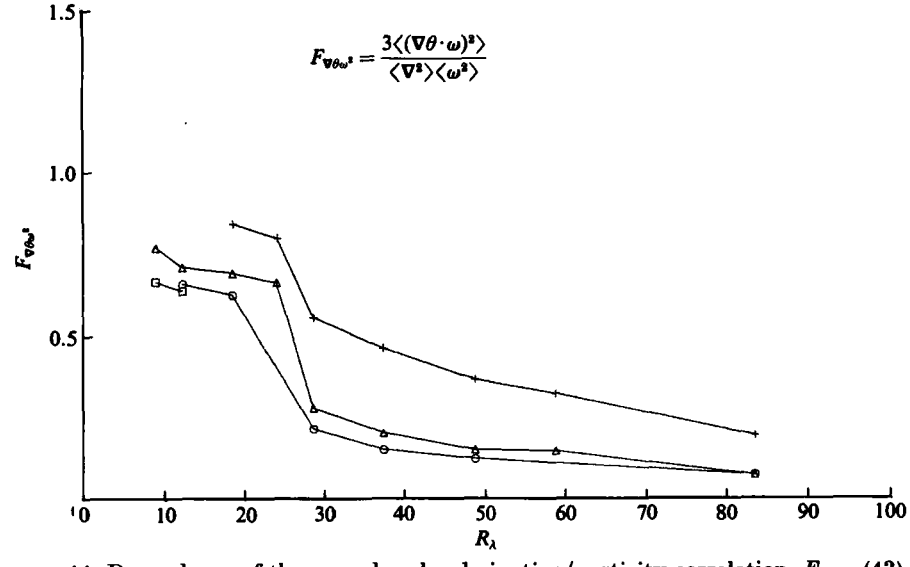

FIGURE 11. Dependence of the second scalar derivative/vorticity correlation, $F_{\nabla\theta\omega 2}$ (43), on Taylor-microscale Reynolds number. For symbols see figure 3.

shows a significant divergence from their uncorrelated values. This is especially true for those with the scalar variance, such as

$$\frac{\langle\theta^4\rangle}{\langle\theta^2\rangle}.$$

For both our simulation and experiment (Sreenivasan *et al.* 1980) the scalar-variance flatness is 3, the Gaussian value. This is expected because, except for mixing, the scalar level is not affected by the dynamics although its derivatives are.

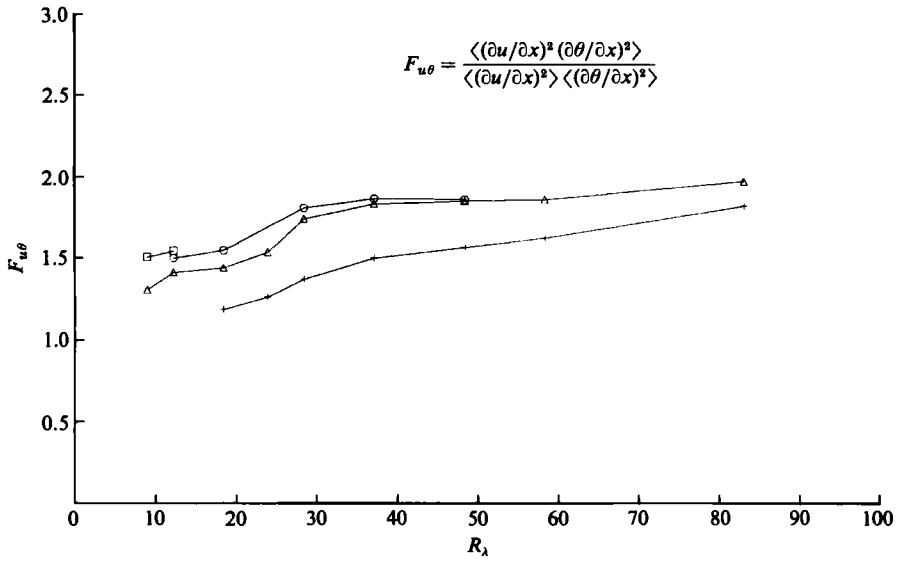

FIGURE 12. Dependence of the mixed scalar/velocity derivative correlation, $F_{u\theta}$ (40), on Taylor-microscale Reynolds number. For symbols see figure 3.

7. Graphics

In Siggia (1981*a*) three-dimensional perspective plots of the vorticity field indicated the presence of vortex tubes. We have produced similar graphics for the vorticity, the scalar gradient, and the compressive component of the rate of strain for a single time from run F19 in figures 13–19. Short lines are used to show the direction of the vector fields. In figures 13(*a*, *b*) the length of each line is proportional to the magnitude of the vorticity and a line is plotted at a grid point only if the magnitude is above a threshold. In figure 13(*a*) the threshold is picked such that only 0.25%, or about 500, of the grid points of a 64^3 mesh are plotted. The 0.25% value was picked so as to allow an assortment of structures to appear, but not so many that the pictures would be cluttered. A strong concentration of vorticity extends most of the way across our computational box. The vorticity in the gap indicated by the circle in figure 13(*a*) is just below the threshold picked. In figure 13(*b*) the threshold is lowered such that 1% of the grid points are plotted and this gap is filled. The circled area in figure 13(*b*) indicates where two tubes might be merging into one. By using a different threshold it is shown that the shape of the structures is not strongly dependent on the sample size.

To show properly the correlations between the fields studied (the vorticity, rate of strain, and scalar gradient), requires colour graphics. In figures 14–19 (plates 1–4) blue is used to represent the vorticity, yellow represents the scalar gradient, and red represents the compressive component of the rate of strain. The vorticity and scalar gradient are conditionally sampled by the same method as in figures 13(*a*, *b*). In figures 14 and 16, 1% of the vorticity points are plotted. In figures 14 and 18, 0.25% of the scalar gradient points are plotted. The projection used for figures 14(*a*), 16(*a*), and 18 is the same as in figures 13(*a*, *b*). Figures 14(*b*) and 16(*b*) represent the same flow fields as figures 14(*a*) and 16(*a*), but rotated 90° about the vertical axis. This rotation shows that the major vortex structure noted in figures 13(*a*, *b*) is a tube in both projections.

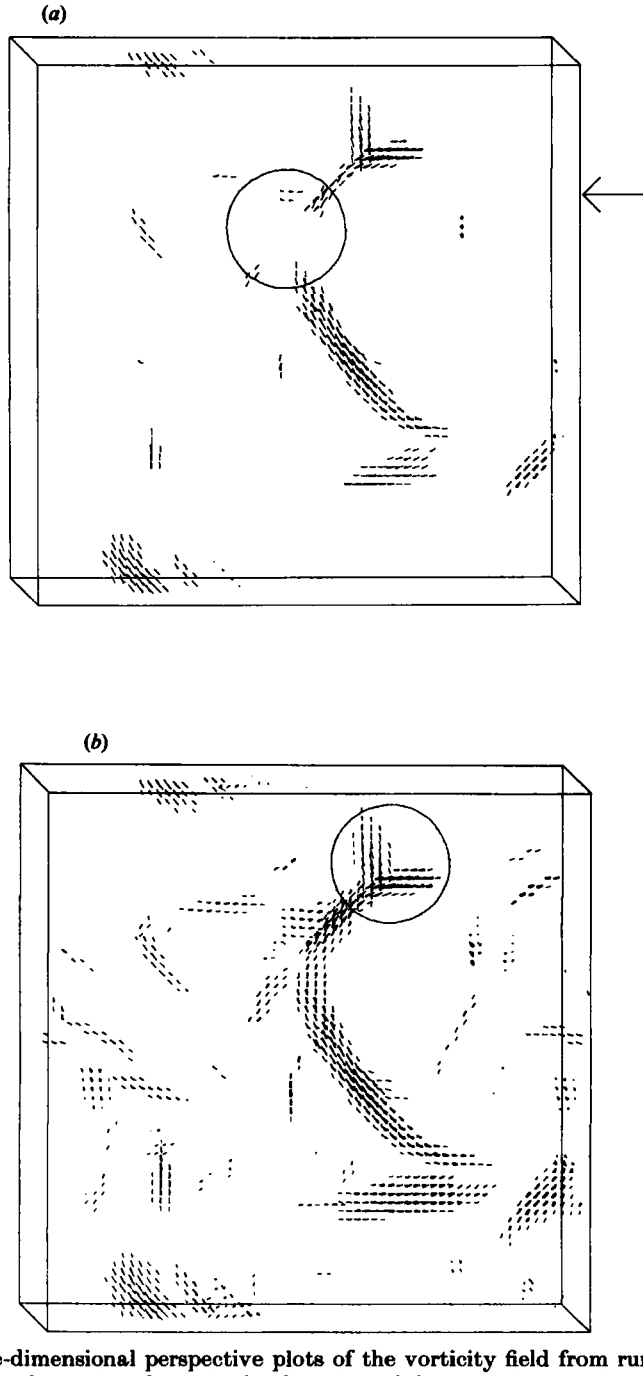

FIGURE 13. Three-dimensional perspective plots of the vorticity field from run F19 ($R_\lambda = 48.5$). Short lines, two mesh spacings long, in the direction of the vorticity are plotted at the points of a 64^3 mesh if the vorticity is above a threshold. (*a*) About 500 lines are plotted. A strong vortex structure extends most of the way across the box. The circle indicates where the vorticity of the structure is just below the threshold. From this perspective the vortex structure appears to be a tube. The arrow indicates where a two-dimensional slice is taken (figures 15, 17 and 19). (*b*) Same perspective as (*a*), but 2000 lines are plotted to show that the vortex structure does extend across the box. The circle indicates where two vortex structures might be merging into one.

The scalar gradient structures in figures 14(*a*, *b*) (plate 1) appear to be sheets when rotated and the scalar gradient in the vicinity of the largest vortex tube is orthogonal to the vorticity, which is consistent with our calculation of $F_{\nabla\theta\omega 2}$ (43). To visualize the correlation between vorticity and scalar gradient better, a two-dimensional slice of figures 14(*a*, *b*) is plotted in figure 15 (plate 2). The location of the slice is indicated by the arrow in figure 13(*a*). Two-dimensional vortex simulations which include scalar markers (Aref & Siggia 1980) and flow-visualization experiments (Winant & Browand 1974; Brown & Roshko 1974) show the scalar marker winding around what are believed to be vortex cores. This winding, and the strong strain around the cores, should lead to strong scalar gradients perpendicular to the vorticity. In figure 15 there are strong scalar gradients wrapped around and perpendicular to the vortex core. This suggests that the scalar in our simulations is also being wound around the vorticity.

Figures 16 (plates 2 and 3) and 18 (plate 4) include the rate of strain. Since the rate of strain is a tensor, it cannot be described with a single line segment. However, by plotting only one of the principal rates of strain at a time, graphics can be produced that show the alignment of the strain field. Figures 16 and 18 conditionally sample, based on the trace of the square of the rate-of-strain tensor (e^2), then plot the principal rate of strain with the largest absolute value; 0.5 % of the grid points are used and in every case the largest principal rate of strain was negative, or compressive, with stretching in the two directions perpendicular to this component to maintain incompressibility. We might expect the largest principal rate of strain to be compressive because the velocity-derivative skewness (14) is negative. That is, by comparing the skewness with one of its isotropic forms (the trace of the rate of strain cubed, 17*a*)), we see that a negative skewness implies a negative value for the largest principal rate of strain.

In figures 16 and 18 there are obvious structures in the rate-of-strain field, but it is not clear from rotation whether these are tubes or sheets. However, there is definite alignment with respect to the vorticity and scalar gradient which is consistent with the calculated statistics. First, because F_2 (33), the correlation between the magnitudes of the rate of strain and vorticity, is large, we expect the rate of strain to be concentrated near the vortex tubes. In figure 16(*a*) the largest strain structure is located near the strong vortex tube. Next, since there will, on the average, be vortex stretching along the tubes, any compressive components should be perpendicular to the tubes. In figure 16(*a*) it appears that the compressive component of the rate of strain is aligned perpendicularly to the vortex tube. This is further illustrated by figure 17 (plate 3), which plots a two-dimensional slice of figures 16(*a*, *b*). The slice is the same as in figure 15. Finally, how do the stretching, or expansive, components of the rate of strain align with the vorticity? A linearized model due to Viellefosse (1982) shows the larger expansive component aligned perpendicular to the vorticity, and the smaller expansive component aligned along the vorticity. Since one of the rotationally invariant forms of the skewness (17*b*) is related to vortex stretching, and both the skewness and F_3 are small, our statistics also suggest that the smaller expansive principal rate of strain is aligned with the vorticity. Unfortunately, we have no graphics that show the expansive components of the rate of strain clearly.

How should the scalar gradient be aligned with respect to the rate of strain? First, the scalar-gradient sheets and rate-of-strain structures should be located near one another because the fourth-order correlations between the rate of strain and scalar gradient (44, 45) are greater than one. Secondly, the scalar gradient should be aligned along the compressive component of the rate of strain because the mixed-derivative skewness is negative. That is, just as we predicted that the largest component of the

rate of strain is compressive by comparing the velocity-derivative skewness with one of its isotropic forms, by comparing the mixed-derivative skewness with its isotropic form (18) we predict that the compressive component of the rate of strain is aligned with the scalar gradient. Comparisons between the scalar gradient and compressive component of the rate of strain in figures 18 and 19 (plate 4) show that both of these predictions are borne out.

8. Discussion

We have studied the derivative correlations of an idealized turbulent flow because they are a quantitative means of probing the small scales of that flow. Numerically, the derivative correlations helped establish the resolution of our simulations. Once the resolution was established, they were compared with experiments and phenomenological models and were used in the interpretation of three-dimensional graphics. Because the small scales of turbulence are believed to be decoupled from the large scales, what is learned about the small scales in this idealized flow should be applicable to turbulent flows in general.

The most important result for the velocity-derivative correlations is that they do not obey the scaling laws predicted by statistical models of intermittency, such as the lognormal model and the β-model. These models predict that the skewness will depend on Reynolds number and that all the fourth-order velocity-derivative correlations will have the same Reynolds-number dependence. In the simulations the skewness does not depend on the Reynolds number and each of the rotationally invariant fourth-order correlations has a different exponent. It is possible that at very high Reynolds numbers the velocity-derivative correlations do behave as these models predict. High-Reynolds-number experiments cited by Tavoularis *et al.* (1978) show the skewness increasing and Van Atta & Antonia (1980) find a different power law for the velocity-derivative flatness at higher Reynolds numbers. Alternatively, models that include the structure of the small scales, such as the model of Tennekes (1968), might be necessary. A simple experiment which might resolve this issue is to find the exponents of more of the fourth-order correlations.

The most important result for the derivative correlations of a passive scalar is that the scalar-derivative flatness is larger than the velocity-derivative flatness. This suggests that the scalar derivative is more intermittent than the velocity derivative and might be related to several other anomalous scalar effects seen experimentally, for example the 'bump' in the scalar spectrum described by Hill (1978) and sharp gradients, or interfaces, called 'ramps' (Antonia *et al.* 1979). What allows sharp structures to form in the scalar field, but not the velocity field? First, they do appear in the velocity field, but as vorticity, which cannot be measured directly, and not as simple velocity gradients, which are easy to measure. These structures are much more likely to be observed in the $\partial u_2/\partial x_1$ field than in $\partial u_1/\partial x_1$, if our conclusions about the relative strengths of I_5 and I_6 (36, 37) are correct.

Graphical display has been used to demonstrate the alignment indicated by the statistics. This shows that the vorticity is concentrated in tubes, not sheets, with large concentrations of the rate of strain and scalar gradient nearby. The statistics and graphics show that the largest principal rate of strain is compressive and aligned perpendicular to the tube. The larger stretching, or expansive, component of the rate of strain also appears to be perpendicular to the vortex tubes, while the stretching along the tubes is small and is probably not caused by the immediate vortex tube. This structure and the statistics are consistent with the linearized model of Viellefosse

(1982) and the structure model of Tennekes (1968), who predicted that the velocity-derivative skewness is independent of Reynolds number. Graphical display also shows that large values of the scalar gradient are wrapped in sheets around the tube and that the gradient is aligned perpendicular to the vorticity and along the compressive component of the rate of strain. This is consistent with correlations between the scalar gradient and both the rate of strain and the vorticity.

Although flow visualization has shown the existence of extended 'coherent' structures on the large scales, most theoretical models of the small scales of turbulence have neglected alignment. They assume that small-scale structures in fully developed turbulence are distributed with random orientation and that statistical mechanics is applicable. Our results suggest that turbulence is characterized by extended vortex tubes and strong alignment between the vorticity and rate of strain. It is possible that as the Reynolds number increases these tubes become more tightly wound and the alignment becomes stronger. There would still be statistics, but the statistics would have to include structures. Strong alignment is not inconsistent with the best-known characteristic of turbulence, the $k^{-\frac{5}{3}}$ spectrum. Lundgren (1982) has shown how fluctuations about a Burger's vortex can give a $k^{-\frac{5}{3}}$ spectrum. Our highest Reynolds number simulation also shows a short $-\frac{5}{3}$ regime. Even if the correlations behave as the statistical phenomenological models predict at higher Reynolds numbers, there should still be a tendency for the vorticity to form tubes and for there to be alignment between the vorticity and rate of strain. The vortex tubes might show more random orientation than in our current graphics, but there would still be strong alignment at the smallest scales.

I wish to thank E. D. Siggia and R. S. Rogallo for assistance in code development and to thank A. Wray and J. R. Herring for many useful discussions. The major portion of this paper was done while I was a National Research Council Associate at NASA Ames Research Center. I also acknowledge initial computational support from the National Center for Atmospheric Research and the support of NSF grant ENG-7902942. The National Center for Atmospheric Research is sponsored by the National Science Foundation.

REFERENCES

ANTONIA, R. A. & CHAMBERS, A. J. 1980 On the correlation between turbulent velocity and temperature derivatives in the atmospheric surface layer. *Boundary-Layer Met.* **18**, 399–410.

ANTONIA, R. A., CHAMBERS, A. J., FRIEHE, C. A. & VAN ATTA, C. W. 1979 Temperature ramps in the atmospheric surface layer. *J. Atmos. Sci.* **36**, 99–108.

ANTONIA, R. A., SATYAPRAKASH, B. R. & HUSSAIN, A. K. M. F. 1982 Statistics of fine-scale velocity in turbulent plane and circular jets. *J. Fluid Mech.* **119**, 55–89.

ANTONIA, R. A. & VAN ATTA, C. W. 1978 Structure functions of temperature fluctuations in turbulent shear flows. *J. Fluid Mech.* **84**, 561–580.

AREF, H. & SIGGIA, E. D. 1980 Vortex dynamics of the two-dimensional turbulent shear layer. *J. Fluid Mech.* **100**, 705–738.

BATCHELOR, G. K. 1952 The effect of homogeneous turbulence on material lines and surfaces. *Proc. R. Soc. Lond.* A **213**, 349–366.

BATCHELOR, G. K. 1959 Small-scale variation of convected quantities like temperature in turbulent fluid. Part 1. General discussion and the case of small conductivity. *J. Fluid Mech.* **5**, 113–133.

BATCHELOR, G. K., HOWELLS, I. D. & TOWNSEND, A. A. 1959 Small-scale variation of convected quantities like temperature in turbulent fluid. Part 2. The case of large conductivity. *J. Fluid Mech.* **5**, 134–139.

BETCHOV, R. 1956 An inequality concerning the production of vorticity in isotropic turbulence. *J. Fluid Mech.* **1**, 497–504.

BROWN, G. L. & ROSHKO, A. 1974 On density effects and large structures in turbulent mixing layers. *J. Fluid Mech.* **64**, 775–816.

CHAMPAGNE, F. H., FRIEHE, C. A., LARUE, J. C. & WYNGAARD, J. C. 1977 Flux measurements, flux estimation techniques and fine-scale turbulence measurements in the unstable surface layer over land. *J. Atmos. Sci.* **34**, 515.

CLAY, J. P. 1973 Turbulent mixing of temperature in water, air and mercury. Ph.D. thesis. University of California at San Diego.

CORRSIN, S. 1951 On the spectrum of isotropic temperature fluctuations in isotropic turbulence. *J. Appl. Phys.* **22**, 469–473.

CORRSIN, S. 1962 Turbulent dissipation fluctuations. *Phys. Fluids* **5**, 1301–1302.

FRENKIEL, F. M. & KLEBANOFF, P. S. 1975 On the lognormality of the small-scale structure of turbulence. *Boundary-Layer Met.* **8**, 173.

FRISCH, U., SULEM, P. L. & NELKIN, M. 1979 A simple model of intermittent fully-developed turbulence. *J. Fluid Mech.* **87**, 719–736.

GIBSON, C. H., STEGEN, G. R. & WILLIAMS, R. B. 1970 Statistics of the fine structure of turbulent velocity and temperature fields measured at high Reynolds number. *J. Fluid Mech.* **41**, 153–167.

GIBSON, C. H. 1968 Fine structure of scalar fields mixed by turbulence. II. Spectral theory. *Phys. Fluids* **11**, 2316–2327.

HERRING, J. R. & KERR, R. M. 1982 Comparison of direct numerical simulations with predictions of two-point closures for isotropic turbulence convecting a passive scalar. *J. Fluid Mech.* **118**, 205–219.

HILL, R. J. 1978 Models of the scalar spectrum for turbulent advection. *J. Fluid Mech.* **88**, 541–562.

KERR, R. M. 1981 Theoretical investigation of a passive scalar such as temperature in isotropic turbulence. Ph.D. thesis; Cooperative Thesis no. 64. Cornell University and National Center for Atmospheric Research.

KERR, R. M. 1983 Higher-order derivative correlations and the alignment of small-scale structures in isotropic numerical turbulence. *NASA Technical Memo* 84407.

KOLMOGOROV, A. N. 1941 Local structure of turbulence in an incompressible fluid at very high Reynolds numbers. *C.R. Acad. Sci. UUSR* **30**, 301–305.

KOLMOGOROV, A. N. 1962 A refinement of previous hypotheses concerning the local structure of turbulence in a viscous incompressible fluid at high Reynolds number. *J. Fluid Mech.* **13**, 82–85.

KUO, A. Y. & CORRSIN, S. 1971 Experiments on internal intermittency and fine-structure distribution functions in fully turbulent fluid. *J. Fluid Mech.* **50**, 285–319.

LARCHEVEQUE, M., CHOLLET, J. P., HERRING, J. R., LESIEUR, M., NEWMAN, G. R. & SCHERTZER, D. 1980 Two-point closure applied to a passive scalar in decaying isotropic turbulence. In *Turbulent Shear Flows* 2 (ed. J. S. Bradbury, F. Durst, B. E. Launder, F. W. Schmidt & J. H. Whitelaw), pp. 50–60. Springer.

LUNDGREN, T. S. 1982 Strained spiral vortex model for turbulent fine structure. *Phys. Fluids* **25**, 2193–2203.

MONIN, A. S. & YAGLOM, A. M. 1975 *Statistical Fluid Mechanics*, vol. 2. Massachusetts Institute of Technology Press.

NELKIN, M. 1981 Do the dissipation fluctuations in high-Reynolds-number turbulence define a universal exponent? *Phys. Fluids* **24**, 556.

NELKIN, M. & BELL, T. L. 1978 One-exponent scaling for very high-Reynolds-number turbulence. *Phys. Rev.* A **17**, 363–369.

ORSZAG, S. A. 1971 Numerical simulation of incompressible flows within simple boundaries: accuracy. *J. Fluid Mech.* **49**, 75–112.

ORSZAG, S. A. & PATTERSON, G. S. 1972 Numerical simulation of turbulence. In *Statistical Models and Turbulence* (ed. M. Rosenblatt & C. Van Atta), Lecture Notes in Physics vol. 12, pp. 127–147. Springer.

PAO, Y-H. 1965 Structure of turbulent velocity and scalar fields at large wavenumbers. *Phys. Fluids* **8**, 1063–1075.

PARK, J. T. 1976 Inertial subrange turbulence measurements in the marine boundary layer. Ph.D. thesis. University of California, San Diego.

PATTERSON, G. S. & ORSZAG, S. A. 1971 Spectral calculations of isotropic turbulence: efficient removal of aliasing interactions. *Phys. Fluids* **14**, 2538–2541.

ROGALLO, R. S. 1981 Numerical experiments in homogeneous turbulence. *NASA TM* 81315.

SAFFMAN, P. G. 1968 Lectures in homogeneous turbulence. In *Topics in Nonlinear Physics* (ed. N. Zabusky), pp. 485–614. Springer.

SIGGIA, E. D. 1981*a* Numerical study of small scale intermittency in three-dimensional turbulence. *J. Fluid Mech.* **107**, 375–406.

SIGGIA, E. D. 1981*b* Invariants for the one-point vorticity and strain rate correlation functions. *Phys. Fluids* **24**, 1934–1936.

SIGGIA, E. D. & PATTERSON, G. S. 1978 Intermittency effects in a numerical simulation of stationary three-dimensional turbulence. *J. Fluid Mech.* **86**, 567–592.

SREENIVASAN, K. R. & TAVOULARIS, S. 1980 On the skewness of the temperature derivative in turbulent flows. *J. Fluid Mech.* **101**, 783–795.

SREENIVASAN, K. R., TAVOULARIS, S., HENRY, R. & CORRSIN, S. 1980 Temperature fluctuations and scales in grid-generated turbulence. *J. Fluid Mech.* **100**, 597–621.

TAVOULARIS, S., BENNETT, S. C. & CORRSIN, S. 1978 Velocity-derivative skewness in small Reynolds number, nearly isotropic turbulence. *J. Fluid Mech.* **88**, 63–69.

TENNEKES, H. 1968 Simple model for the small-scale structure of turbulence. *Phys. Fluids* **11**, 669–671.

VAN ATTA, C. W. 1974 Influence of fluctuations in dissipation rates on some statistical properties of turbulent scalar fields. *Izv. Atmos. Ocean Phys.* **10**, 712–719.

VAN ATTA, C. W. & ANTONIA, R. A. 1980 Reynolds-number dependence of skewness and flatness factors of turbulent velocity derivatives. *Phys. Fluids* **23**, 252–257.

VIEILLEFOSSE, P. 1982 Local interaction between vorticity and shear in a perfect incompressible fluid. *J. de Physique* **43**, 837–842.

WARHAFT, Z. & LUMLEY, J. L. 1978 An experimental study of the decay of temperature fluctuation in grid-generated turbulence. *J. Fluid Mech.* **88**, 659–684.

WINANT, C. D. & BROWAND, F. K. 1974 Vortex pairing: the mechanism of turbulent mixing layer growth at moderate Reynolds number. *J. Fluid Mech.* **63**, 237–255.

WRAY, A. 1981 Very low storage time-advancement schemes. NASA Ames Research Center, private communication.

WYNGAARD, J. C. 1971 The effect of velocity sensitivity on temperature derivative statistics in isotopic turbulence. *J. Fluid Mech.* **48**, 763–769.

WYNGAARD, J. C. & TENNEKES, H. 1970 Measurements of the small-scale structure of turbulence at moderate Reynolds numbers. *Phys. Fluids* **13**, 1962–1969.

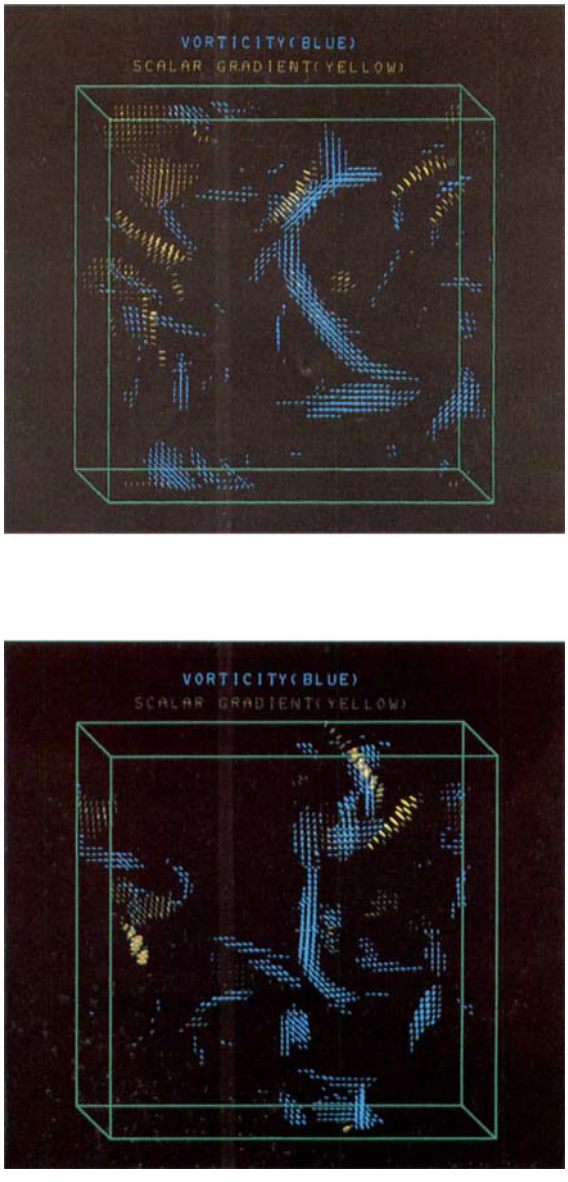

FIGURE 14. Three-dimensional perspective plots of the vorticity (blue) and scalar-gradient (yellow) fields. Short lines in the direction of the scalar gradient are plotted at the points of a 64^3 mesh if the scalar gradient is above a threshold. 500 lines are plotted for the scalar gradient. 2000 lines are plotted for the vorticity. (*a*) The same perspective as in figures 13(*a*, *b*). The scalar-gradient structure in the top centre is aligned along with the vortex structure with the scalar gradient perpendicular to the vorticity. This scalar-gradient structure is a sheet seen edge on. Two scalar structures in the upper-left corner are sheets seen from the top down. (*b*) The same field as (*a*), but rotated 90° about the vertical axis. In the middle the vortex structure continues to look like a tube. In the upper right it appears more twisted. The scalar-gradient structure in (*a*) which is aligned with the vorticity is the fanlike structure in the upper centre. The scalar-gradient structures to the right and above the fanlike structure are the sheets in the upper-left corner in (*a*), but now seen edge on.

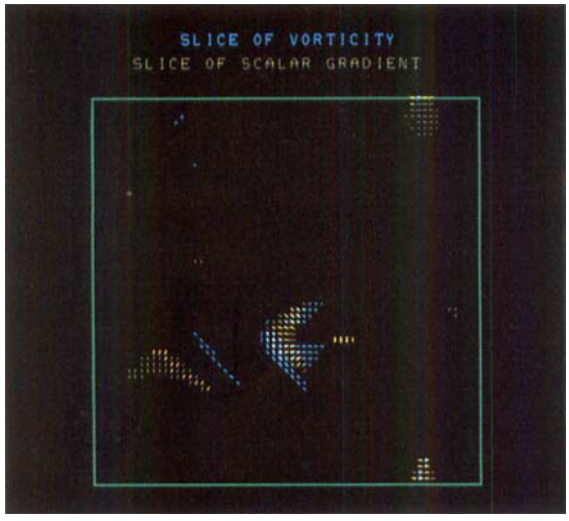

FIGURE 15. Two-dimensional slice of figures 14(*a*, *b*) as indicated by the arrow in figure 13(*a*). The vortex structure in the centre might be associated with vortex merging. The scalar-gradient structure in the centre is partially wrapped around the vortex structure and shows the scalar gradient aligned perpendicular to the vorticity.

FIGURE 16. For legend see opposite.

FIGURE 16. Three-dimensional perspective plots of the vorticity (blue) and compressive component of the rate-of-strain (red) fields. Short lines in the direction of the compressive component are plotted at the points of a 64^3 mesh if the total rate of strain is above a threshold. 1000 lines are plotted for the rate of strain. 2000 lines are plotted for the vorticity. (*a*) The same perspective as in figures 13 (*a*) and 14 (*a*). The rate-of-strain structure in the top centre is aligned along the vortex structure with the compressive component of the rate of strain perpendicular to the vorticity. (*b*) The same field as (*a*), but rotated 90° about the vertical axis. It has the same perspective as figure 14 (*b*). The rate-of-strain in (*a*) which is aligned with the vorticity is the fanlike structure in the upper centre.

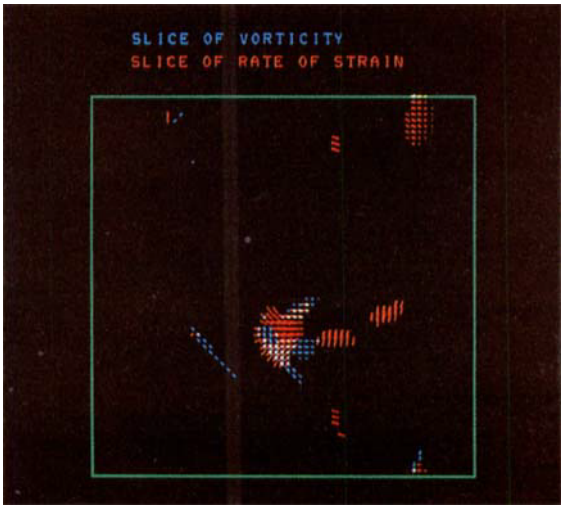

FIGURE 17. Two-dimensional slice of figures 16 (*a*, *b*) indicated by the arrow in figure 13 (*a*). The structures in the centre show the compressive component of the rate of strain aligned perpendicular to the vorticity.

FIGURE 18. Three-dimensional perspective plots of the compressive component of the rate-of-strain (red) and scalar-gradient (yellow) fields. 1000 lines are plotted for the rate of strain. 500 lines are plotted for the scalar gradient. The perspective is the same as in figures 13(*a*) and 14(*a*). The rate-of-strain structure in the top centre is aligned along the scalar-gradient structure with the compressive component of the rate of strain parallel to the scalar gradient.

FIGURE 19. Two-dimensional slice of figure 18 indicated by the arrow in figure 13(*a*). The structures in the centre show the compressive component of the rate of strain aligned parallel to the scalar gradient.